Techniques for Analyzing Frequency Selective Surfaces—A Review

RAJ MITTRA, FELLOW, IEEE, CHI H. CHAN, MEMBER, IEEE, AND TOM CWIK

Invited Paper

In this paper we discuss a number of representative techniques for analyzing Frequency Selective Surfaces (FSSs), which comprise periodic arrays of patches or apertures in a conducting screen and find important applications as filters in microwaves and optics. We review the basic properties of the FSSs and describe several different approaches to predicting their frequency response characteristics. Some recent developments in the treatment of truncated, curved, and doubly periodic screens are mentioned and representative results are included.

I. INTRODUCTION

Frequency Selective Surfaces (FSSs), which find widespread applications as filters for microwaves and optical signals, have been the subject of extensive studies in recent years. These surfaces comprise periodically arranged metallic patch elements or aperture elements within a metallic screen and exhibit total reflection (patches) or transmission (apertures) in the neighborhood of the element resonance. Typical FSS geometries are shown in Fig. 1. The reflection or transmission band is predicted by analyzing the surface using techniques which are efficient and which can model a wide range of configurations. In this paper, techniques currently used in this analysis are reviewed. The techniques are used in the design of FSSs and, as outlined in the last section of this paper, are the basis for research into related structures.

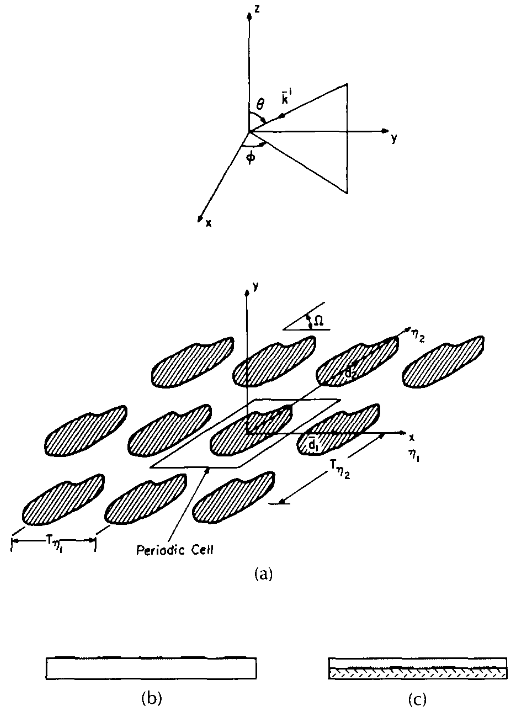

Fig. 1. Geometry of frequency selective screen. (a) Freestanding FSS. (b) FSS with a dielectric substrate. (c) FSS with both a dielectric substrate and a superstrate.

Historically,[1] the understanding of the principles underlying the physics of frequency selective surfaces has directly evolved from the investigation of diffraction gratings in optics which are used to decompose a beam of nonmonochromatic light into its spectral orders. This filtering process, as well as the diffraction grating itself, was discovered by the American physicist David Rittenhouse, as documented by an engaging scientific exchange between Francis Hopkinson and Rittenhouse published in 1786 [1]. The exchange began the previous year when Hopkinson, writing Rittenhouse, described a curious phenomenon he had recenty observed and requested that Mr. Rittenhouse devote his attention to it. He wrote, "*Sitting at my door one evening last summer, I took a silk handkerchief out of my pocket, and stretching a portion of it tight between my two hands, I held it up before my face and viewed, through the*

Manuscript received May 23, 1988; revised September 30, 1988. The work at the University of Illinois was supported in part by the Joint Services Electronics Program at the Coordinated Science Laboratory under Grant N00014-81-C-0149.

R. Mittra and C. H. Chan are with the Electromagnetic Communication Laboratory, Department of Electrical and Computer Engineering, University of Illinois, Urbana, IL 61801, USA.

T. Cwik is with the Jet Propulsion Laboratory, California Institute of Technology, Pasadena, CA 91109, USA.

IEEE Log Number 8825167.

[1] The historical account of the development of frequency selective surface has been previously described by Cwik [40].

0018-9219/88/1200-1593$01.00 © 1988 IEEE

handkerchief, one of the street lamps which are about one hundred yards distant; . . . I observed the silk threads magnified to the size of coarse wires; but was much surprised to find that, although I moved the handkerchief to the right and left before my eyes, the dark bars did not seem to move at all, but remained permanent before the eye." Rittenhouse, taking interest in this phenomenon, read his results before the American Philosophical Society. He began, "*The experiment you mention, with a silk handkerchief and the distant flame of a lamp, is much more curious than one would at first imagine.*" Constructing his own apparatus from equally spaced hairs Rittenhouse held the grating up to light and observed, "*I saw three parallel lines, almost equal in brightness, and on each side four or five others much fainter and growing more faint, coloured and indistinct.*" A more exacting grating was constructed, changing the spacing of the hairs with the following results, "*The three middle lines of light were now not so bright as they had been before, but the others were stronger and more distinct, and I could count six on each side of the middle line, seeming to be equally distant from each other, estimating the distance from the centre of one to the centre of the next . . . The others were more indistinct, and consisted each of the prismatic colours.*" Rittenhouse was observing the filtering of white light into distinct wavelength bands (colored lines), which were equally spaced from the center line of white (unfiltered) light—the spacing depending upon the spacings between hairs. Because of the simplicity of this filtering process, the diffraction grating and related structures have been extended to many areas of engineering and science.

The phenomenon described by Rittenhouse is also fundamental to any screen consisting of periodically placed patches or perforated periodically with holes. The change of structure though increases the complexity in understanding and analyzing the screen which now varies in two dimensions. The configuration of each element (either patch or aperture within an array of periodic cells), as well as the spacing, will contribute to the form of the scattered fields—transmitted or reflected. Similarly, because of the finite nature of the element, the scattered field will exhibit resonances as the excitation wavelength is varied, i.e., the fields will either be totally reflected or transmitted for patch or aperture screens, respectively, at a specific wavelength. The resonances will generally occur when the size of the element is an integer number of half wavelengths, with the infinite array of elements modifying the spectral response from what it would be if it were isolated. For wavelengths near the first resonance, a distinct spectral response associated with the element will be observed. At wavelengths past the first resonance, the diffracted orders begin scattering energy at regular angles as described above by Rittenhouse for the grating, and as the wavelength is decreased, repeated resonances occur. Finally, the fraction of transmitted power approaches the fraction of the aperture area within the periodic cell in the limit of zero wavelength.

II. TYPICAL APPLICATION OF FSSS

The applications of frequency selective surfaces are many and varied, and they range over much of the electromagnetic spectrum. In the microwave region, the frequency selective properties of periodic screens are exploited, for example, to make a more efficient use of reflector antennas [2]. As shown in Fig. 2, a frequency selective surface is placed between two feeds, radiating at differing frequencies, and the main reflector. The screen is totally reflecting (or nearly so) over the operating band of feed one, and conversely, it is nearly totally transparent over the band of feed two. Hence, in this configuration, two independent feeds may share the same reflector antenna simultaneously, in a frequency reuse mode. The desired spectral response of the screen is shown in Fig. 3 for a single angle of incidence and polarization of the incident field. Though this response may meet the requirements of the reflector system when the incident angle on the screen is near normal, changing the angle of incidence or polarization of the feed excitation may degrade the spectral response of the screen to a point where the antenna characteristics no longer meet the system requirements. Hence, a patch geometry that produces a response that is relatively insensitive to the angle of incidence of the illuminating field is highly desired. The Jerusalem cross geometry [3] has been found to be one of the promising candidates as an FSS element satisfying this criterion.

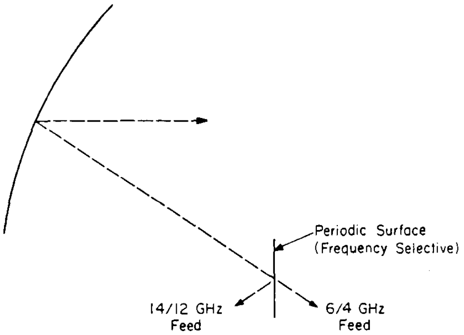

Fig. 2. Reflector antenna system using frequency selective screen.

A second example of the exploitation of the frequency selective property of periodic screens in the microwave region is the application in radome design [4]. The screen can be tuned to provide a bandpass transmission characteristic at the operating frequency of the antenna. At the out-of-band frequencies, the screen can be made essentially totally reflecting, and the radome can be designed to blend with the skin of the vehicle such that minimal scattering occurs at the joint between the radome and the skin.

In the far-infrared region, periodic screens are used as polarizers, beam splitters, as well as mirrors for improving the pumping efficiency in molecular lasers [5], [6]. A polarizer can be constructed from a diffraction grating such that the fields polarized parallel to the grating are reflected, while those with an orthogonal polarization are transmitted. A cavity mirror used in a laser can be constructed from a frequency selective surface such that it is totally reflecting at the wavelength of the energy used to pump the cavity, and partially transmitting (0–40 percent) at the lasing wavelength. No energy used in optically pumping the laser is lost

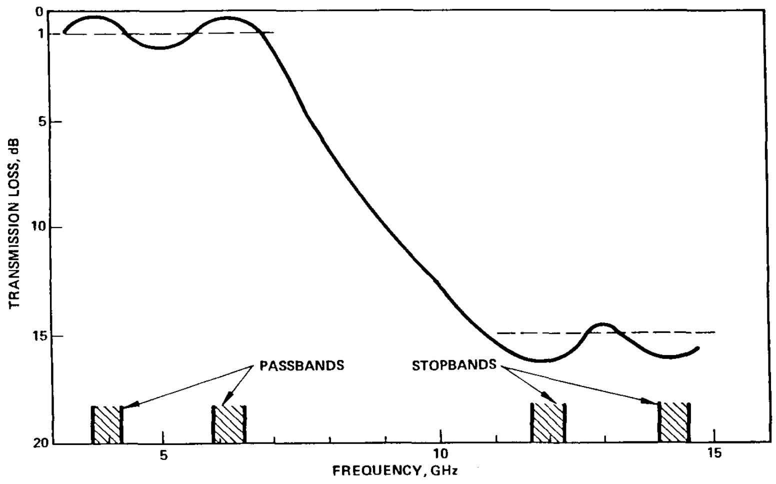

Fig. 3. Spectral response of screen used in Fig. 2.

at the mirror; hence, the efficiency of the system is increased.

Another application of the FSS in this wavelength range is in infrared sensors where, once again, the frequency selective property of the FSS is used to absorb the desired frequencies in the substrate material backing the screen, while the out-of-band frequencies are rejected.

In the near-infrared and visible portions of the spectrum, periodic screens have been proposed as solar selective surfaces to aid in the collection of solar energy [7]. A screen can be designed such that it is essentially transparent in the frequency band where the solar cells are most efficient and is reflecting at frequencies outside this band. Finally, natural occurrences of periodic screens have been discovered in entomological studies [8], e.g., in the corneas of insects—the well-known fly-eye lens. More applications of FSSs can be found in [8]–[12].

III. FORMULATION OF THE FSS SCATTERING PROBLEM

The first step in formulating the problem of electromagnetic scattering from a frequency selective surface is to relate the fields scattered from the FSS to the surface currents induced on the screen by the incident field. Throughout this paper, we will assume that the FSS is infinitesimally thin, an assumption which is usually valid for most applications, even at optical frequencies. Initially, we consider the case a freestanding, perfectly conducting FSS whose geometry is shown in Fig. 1(a) [13]–[16]. Later in this paper we indicate how this formulation can be modified to handle an FSS on a dielectric substrate, and with a finite conductivity.

Let $\boldsymbol{J}$ be the induced surface current density on the FSS and $\boldsymbol{A}$ be the magnetic vector potential due to this current. In general, due to the planar nature of the FSS, the induced surface current $\boldsymbol{J}$ has only nonzero transverse components. Assuming that the time convention is exp $(j\omega t)$, one can relate the transverse (to z) components of $\boldsymbol{A}$ and $\boldsymbol{J}$ as follows

$$\begin{bmatrix} A_x(x, y) \\ A_y(x, y) \end{bmatrix} = \bar{\bar{G}}(x, y) * \begin{bmatrix} J_x(x, y) \\ J_y(x, y) \end{bmatrix} \tag{1}$$

where

$$\bar{\bar{G}} = \frac{\exp(-jk_0 r)}{4\pi r}\bar{\bar{I}}, \quad r = (x^2 + y^2)^{1/2},$$

$$k_0 = \text{free-space wave number},$$

$$\bar{\bar{I}} = \text{identity tensor},$$

and $*$ is the convolution operator.

The next step is to express the transverse components of the scattered electric field $\boldsymbol{E}^s$ in the plane of the screen, i.e., at $z = 0$, in terms of the transverse components of the vector potential $\boldsymbol{A}$. The relationship is given by

$$\begin{bmatrix} E_x^s \\ E_y^s \end{bmatrix} = \frac{1}{j\omega\epsilon_0}\begin{bmatrix} \frac{\partial^2}{\partial x^2} + k_0 & \frac{\partial^2}{\partial x \partial y} \\ \frac{\partial^2}{\partial x \partial y} & \frac{\partial^2}{\partial y^2} + k_0 \end{bmatrix}\begin{bmatrix} A_x \\ A_y \end{bmatrix}. \tag{2}$$

In order to take full advantage of the periodicity of the geometry, it is convenient to rewrite the above equation in the spectral domain [3], [17]. To this end, we use Fourier transform (2) to obtain

$$\begin{bmatrix} \tilde{E}_x^s(\alpha, \beta) \\ \tilde{E}_y^s(\alpha, \beta) \end{bmatrix} = \frac{1}{j\omega\epsilon_0}\begin{bmatrix} k_0 - \alpha^2 & -\alpha\beta \\ -\alpha\beta & k_0 - \beta^2 \end{bmatrix}\tilde{\bar{\bar{G}}}(\alpha, \beta)\begin{bmatrix} \tilde{J}_x(\alpha, \beta) \\ \tilde{J}_y(\alpha, \beta) \end{bmatrix} \tag{3}$$

where

$$\tilde{\bar{\bar{G}}}(\alpha, \beta) = \frac{-j}{2(k_0^2 - \alpha^2 - \beta^2)^{1/2}}\bar{\bar{I}}$$

and α and β are the transform variables corresponding to the x and y coordinates, respectively. When the FSS is strictly doubly periodic (which requires that it be of infinite extent), the Fourier transform of the induced current $\boldsymbol{J}$ is nonzero only for an infinite set of discrete values of the spectral variables α and β. These values, designated here as α_{mn} and β_{mn}, are associated with the Floquet harmonics for the doubly periodic screen, named after the nineteenth century French mathematician Floquet who introduced the concepts of these harmonics in the context of his work on the periodic solution of differential equations. The explicit expressions for α_{mn} and β_{mn} are as follows:

$$\alpha_{mn} = \frac{2\pi m}{a} + k_0 \sin\theta \cos\phi$$

$$\beta_{mn} = \frac{2\pi n}{b \sin\Omega} - \frac{2\pi m}{a} \cot\Omega + k_0 \sin\theta \sin\phi.$$

where θ, ϕ are the angles of the incident plane wave. In Fig. 1 a is T_{η_1}, and b is T_{η_2}.

Taking the inverse transform of (3) and enforcing the boundary condition that the total field, i.e., the sum of the scattered field and the incident field, be zero on the perfectly conducting surface of the FSS, we obtain the following equation for the unknown induced currents on the screen

$$\frac{1}{j\omega\epsilon_0} \sum_m \sum_n \begin{bmatrix} k_0^2 - \alpha_{mn}^2 & -\alpha_{mn}\beta_{mn} \\ -\alpha_{mn}\beta_{mn} & k_0^2 - \beta_{mn}^2 \end{bmatrix} \cdot \bar{\bar{\tilde{\mathbf{G}}}}(\alpha_{mn}, \beta_{mn}) \begin{bmatrix} \tilde{J}_x(\alpha_{mn}, \beta_{mn}) \\ \tilde{J}_y(\alpha_{mn}, \beta_{mn}) \end{bmatrix} e^{j(\alpha_{mn}x + \beta_{mn}y)}$$
$$= \sum_m \sum_n \begin{bmatrix} \tilde{G}_{xx} & \tilde{G}_{xy} \\ \tilde{G}_{yx} & \tilde{G}_{yy} \end{bmatrix} \begin{bmatrix} \tilde{J}_x(\alpha_{mn}, \beta_{mn}) \\ \tilde{J}_y(\alpha_{mn}, \beta_{mn}) \end{bmatrix} e^{j(\alpha_{mn}x + \beta_{mn}y)}$$
$$= -\begin{bmatrix} E_x^i(x, y) \\ E_y^i(x, y) \end{bmatrix}. \tag{4}$$

The transformed derivatives and the constant $1/j\omega\epsilon_0$ have been incorporated into the individual components of $\bar{\bar{G}}$ to simplify the notation. Once the induced currents have been determined by solving the above set of equations, other quantities of practical interest, e.g., reflection and transmission coefficients for the dominant harmonics, as well as the scattering matrix description for the screen, can be readily calculated.

For an aperture-type (inductive) FSS [18]–[20], we can apply the concepts of duality to (4) by replacing $\boldsymbol{E}$ with $\boldsymbol{H}$ and ϵ_0 and μ_0. Furthermore, invoking the symmetry of the screen geometry, and defining a magnetic current $\boldsymbol{K}$ in terms of the aperture field $\boldsymbol{E}^a$ as

$$\boldsymbol{K} = \boldsymbol{E}^a \times \hat{z} \tag{5}$$

we can obtain the following equation for the transverse components of $\boldsymbol{E}^a$

$$\frac{2}{-j\omega\mu_0} \sum_m \sum_n \begin{bmatrix} \alpha_{mn}\beta_{mn} & k_0^2 - \alpha_{mn}^2 \\ -k_0^2 + \beta_{mn}^2 & -\alpha_{mn}\beta_{mn} \end{bmatrix} \bar{\bar{\tilde{\mathbf{G}}}}(\alpha_{mn}, \beta_{mn})$$
$$\cdot \begin{bmatrix} E_x^a(\alpha_{mn}, \beta_{mn}) \\ E_y^a(\alpha_{mn}, \beta_{mn}) \end{bmatrix} e^{j(\alpha_{mn}x + \beta_{mn}y)} = \begin{bmatrix} H_x^i \\ H_y^i \end{bmatrix}. \tag{6}$$

The solution of the above equation yields the unknown field distribution in the aperture of an inductive FSS. We hasten to add, however, that the above equation is strictly valid only for a perfectly conducting FSS. If the screen has a finite conductivity, we must formulate the problem in terms of the surface currents on the conducting portions of the screen, rather than the fields in the aperture.

Of considerable practical interest are the extensions of the formulations presented above for the patch and aperture-type FSSs to the cases of screens i) embedded in a dielectric medium of finite thickness; ii) printed on a substrate; and iii) with both a substrate and a superstrate [21]–[24]. We now show below how these could be carried out in a relatively straightforward manner by following the procedure outlined below. Consider an FSS structure with a dielectric substrate and superstrate shown in Fig. 1(c). To modify the operator equation derived earlier for the induced current on the freestanding screen, we simply replace the spectral dyadic Green's function in (4) with a new composite Green's function which accounts for both the substrate and the superstrate. The spectral dyadic Green's function for a layered dielectric medium can be conveniently obtained via the spectral domain immittance approach, which has been described in [25] in connection with printed circuit transmission line problems.

Following the notation in [25], and again denoting the surface current densities by J_x and J_y, the operator equation relating the current densities and the transverse components of the incident field on the conducting surface can be written as

$$-\begin{bmatrix} E_x^i(x, y) \\ E_y^i(x, y) \end{bmatrix} = \sum_m \sum_n \begin{bmatrix} \tilde{G}_{xx}^e & \tilde{G}_{xy}^e \\ \tilde{G}_{yx}^e & \tilde{G}_{yy}^e \end{bmatrix} \begin{bmatrix} \tilde{J}_x(\alpha_{mn}, \beta_{mn}) \\ \tilde{J}_y(\alpha_{mn}, \beta_{mn}) \end{bmatrix} e^{j(\alpha_{mn}x + \beta_{mn}y)} \tag{7}$$

where

$$\begin{bmatrix} \tilde{G}_{xx}^e & \tilde{G}_{xy}^e \\ \tilde{G}_{yx}^e & \tilde{G}_{yy}^e \end{bmatrix} = \begin{bmatrix} \tilde{Z}^e \cos^2\theta + \tilde{Z}^h \sin^2\theta & (\tilde{Z}^e - \tilde{Z}^h) \sin\theta \cos\theta \\ (\tilde{Z}^e - \tilde{Z}^h) \sin\theta \cos\theta & \tilde{Z}^e \sin^2\theta + \tilde{Z}^h \cos^2\theta \end{bmatrix} \tag{8}$$

$$\tilde{Z}^{e,h} = \frac{1}{Y^{+e,h} + Y^{-e,h}}$$

$$Y^{+e,h} = Y_1^{e,h} \frac{Y_1^{e,h} + Y_0^{e,h} \coth\gamma_1 t_1}{Y_1^{e,h} \coth\gamma_1 t_1 + Y_0^{e,h}},$$

$$Y^{-e,h} = Y_2^{e,h} \frac{Y_2^{e,h} + Y_0^{e,h} \coth\gamma_2 t_2}{Y_2^{e,h} \coth\gamma_2 t_2 + Y_0^{e,h}}$$

$$Y_i^e = -j\omega \frac{\epsilon_0\epsilon_{ri}}{\gamma_i}, \quad Y_i^h = -\frac{\gamma_i}{j\omega\mu_0},$$

$$\gamma_i = (\alpha_{mn}^2 + \beta_{mn}^2 - \epsilon_{ri}k_0^2)^{1/2},$$

$$\cos\theta = \frac{\alpha_{mn}}{(\alpha_{mn}^2 + \beta_{mn}^2)^{1/2}}, \quad \sin\theta = \frac{\beta_{mm}}{(\alpha_{mn}^2 + \beta_{mn}^2)^{1/2}}.$$

The transverse components of the incident field on the conducting surface are derived by constructing the z-directed vector potential in each of the dielectric layered regions (see Fig. 4). Enforcing the appropriate continuity conditions at each dielectric interface, we can obtain the following two expressions for the incident field on the conducting surface for the transverse electric (TE) and trans-

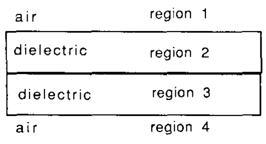

Fig. 4. Stratified regions in which the vector potentials are derived.

verse magnetic (TM) cases, respectively:

$$\begin{bmatrix} E_x^i \\ E_y^i \end{bmatrix} = j(R_1 + R_2)e^{j(\alpha x + \beta y)} \begin{bmatrix} -\beta \\ \alpha \end{bmatrix} \quad \text{—TE} \tag{9a}$$

$$\begin{bmatrix} E_x^i \\ E_y^i \end{bmatrix} = \frac{\gamma_1}{\omega\epsilon_{r1}\epsilon_0}(R_1 - R_2)e^{j(\alpha x + \beta y)} \begin{bmatrix} \alpha \\ \beta \end{bmatrix} \quad \text{—TM} \tag{9b}$$

where

$$R_1 = \frac{\gamma_0(e^{\gamma_0 t_1}/\sinh \gamma_1 t_1)[(\bar{\gamma}_2^2 + \gamma_0\bar{\gamma}_1 + (\gamma_0 + \bar{\gamma}_1)\bar{\gamma}_2 \coth \gamma_2 t_2]}{D}$$

$$R_2 = -\frac{\gamma_0(e^{\gamma_0 t_1}/\sinh \gamma_1 t_1)[(\bar{\gamma}_2^2 - \gamma_0\bar{\gamma}_1 + (\gamma_0 - \bar{\gamma}_1)\bar{\gamma}_2 \coth \gamma_2 t_2]}{D}$$

$$\begin{aligned} D = {} & (\gamma_0 + \bar{\gamma}_1^2)\bar{\gamma}_2 \coth \gamma_2 t_2 + (\gamma_0^2 + \bar{\gamma}_2^2)\bar{\gamma}_1 \\ & \cdot \coth \gamma_1 t_1 + (\bar{\gamma}_1^2 + \bar{\gamma}_2^2)\gamma_0 \\ & + 2\gamma_0\bar{\gamma}_1\bar{\gamma}_2 \coth \gamma_2 t_2 \coth \gamma_1 t_1 \end{aligned}$$

$$\bar{\gamma}_i = \begin{Bmatrix} \gamma_i & \text{—TE} \\ \gamma_i/\epsilon_{ri} & \text{—TM} \end{Bmatrix}.$$

Using the above expressions for the incident fields and that of the dyadic Green's function given in (8) in the operator equation for the induced current density, one obtains the desired equation (7) to be solved for an FSS with substrates and superstrates. Note that the format of this equation is identical to that of the freestanding screen, although modifications are introduced by the expressions for the incident field and the composite Green's function.

When the surface conductivity is finite, the total electric field on the screen no longer vanishes, and it becomes necessary to modify (4) and (7) in order to satisfy the new, impedance type of boundary condition [26]–[29]. For a thin surface, the total electric field on the surface is equal to the product of the surface impedance and the surface current density. This impedance boundary condition can be represented by the following equation:

$$\begin{bmatrix} E_x^s \\ E_y^s \end{bmatrix} + \begin{bmatrix} E_x^i \\ E_y^i \end{bmatrix} - Z_s \begin{bmatrix} J_x \\ J_y \end{bmatrix} = 0 \tag{10}$$

where Z_s is the sheet impedance of the infinitely thin surface. Using the impedance boundary condition of (10), (4) and (7) are modified to treat finite conductivity surfaces as follows:

$$\begin{aligned} -\begin{bmatrix} E_x^i(x, y) \\ E_y^i(x, y) \end{bmatrix} = {} & \sum_m \sum_n \begin{bmatrix} \tilde{G}_{xx} & \tilde{G}_{xy} \\ \tilde{G}_{yx} & \tilde{G}_{yy} \end{bmatrix} \begin{bmatrix} \tilde{J}_x(\alpha_{mn}, \beta_{mn}) \\ \tilde{J}_y(\alpha_{mn}, \beta_{mn}) \end{bmatrix} \\ & \cdot e^{j(\alpha_{mn}x + \beta_{mn}y)} - Z_s \begin{bmatrix} J_x \\ J_y \end{bmatrix} \\ & \text{—for the free-standing FSS} \end{aligned} \tag{11}$$

$$\begin{aligned} -\begin{bmatrix} E_x^i(x, y) \\ E_y^i(x, y) \end{bmatrix} = {} & \sum_m \sum_n \begin{bmatrix} \tilde{G}_{xx}^e & \tilde{G}_{xy}^e \\ \tilde{G}_{yx}^e & \tilde{G}_{yy}^e \end{bmatrix} \begin{bmatrix} \tilde{J}_x(\alpha_{mn}, \beta_{mn}) \\ \tilde{J}_y(\alpha_{mn}, \beta_{mn}) \end{bmatrix} \\ & \cdot e^{j(\alpha_{mn}x + \beta_{mn}y)} - Z_s \begin{bmatrix} J_x \\ J_y \end{bmatrix} \\ & \text{—for FSS embedded in dielectrics.} \end{aligned} \tag{12}$$

An approach to solving the operator equations for the induced surface current or the aperture field, from which useful parameters such as the transmission and reflection coefficients of different FSS structures can be calculated under various conditions of illumination, is to use the method of moments [30] and convert them into matrix equations. The details of this procedure are given in the next section.

IV. SOLUTION OF OPERATOR EQUATION

In this section, we discuss the solution of the equations governing the characteristics of FSS derived in the previous section using the moment method.

As a first step we rewrite (11) and (12) in a symbolic form

$$\boldsymbol{L} * \boldsymbol{u} = \boldsymbol{g} \tag{13}$$

where $\boldsymbol{u}$ represents either the unknown induced current $\boldsymbol{J}$ or the aperture field $\boldsymbol{E}^a$ (depending upon whether we are solving the patch or aperture type FSS problem), $\boldsymbol{g}$ corresponds to the known incident $\boldsymbol{E}^i$ or $\boldsymbol{H}^i$ field, and $\boldsymbol{L}$ is the operator relating the unknown $\boldsymbol{u}$ to the incident field. The moment method begins by expressing the unknown $\boldsymbol{u}$ in terms of a set of basis functions $\boldsymbol{f}$'s as

$$\boldsymbol{u} = \sum_i C_i \boldsymbol{f}_i \tag{14}$$

where the Cs are the unknown coefficients yet to be determined. Substituting (14) into (13) and using $\boldsymbol{f}$'s as the testing functions, (13) is transformed into the following matrix equation

$$\left[\boldsymbol{f}_j, \sum_i C_i \boldsymbol{L} * \boldsymbol{f}_i\right] = [\boldsymbol{f}_j, \boldsymbol{g}], \qquad j = 1, 2, \cdots \tag{15}$$

where the scalar product $[\boldsymbol{a}, \boldsymbol{b}]$ is defined as

$$[\boldsymbol{a}, \boldsymbol{b}] = \int_{\text{plate}} \boldsymbol{a}^* \cdot \boldsymbol{b}\, ds \qquad \text{for patch}$$

$$[\boldsymbol{a}, \boldsymbol{b}] = \int_{\text{aperture}} \boldsymbol{a}^* \times \boldsymbol{b} \cdot \hat{z}\, ds \qquad \text{for aperture}$$

and $\boldsymbol{a}^*$ is the complex conjugate of $\boldsymbol{a}$.

The efficiency with which the solution of (11) and (12) can be derived for a desired accuracy depends critically upon the choice of the basis functions. It is helpful to consider several factors in choosing these functions. First, in order that the number of basis functions used to represent the unknown current be minimal, and therefore the matrix size be small, it is desirable that these functions satisfy the appropriate edge condition [31]. Second, it is convenient to choose the basis functions that are analytically Fourier transformable so that the need to derive their transform numerically is obviated when using the operator equations (11) and (12) in the transform domain. Third, in order that the scalar products appearing in the matrix elements be calculable without an inordinately large investment in computer time, the transforms of the basis functions must decay reasonably rapidly for large α and β. A fourth factor to keep in mind is that if the number of basis functions needed to accurately represent the unknown current density (or aperture field) becomes too large for the core memory of the computer, then a solution scheme that is different from the Gaussian elimination method, such as an iterative procedure, must be utilized, often at greatly increased cost in terms of computer time.

In general, there are two categories of basis functions used to represent the unknown function in the context of the moment method, viz., the entire domain and subdomain basis functions and we discuss them both in the following. Consider the entire domain functions first. These functions span the entire support of the unknown, the patch or the aperture in an FSS cell, and are typically tailored for the specific geometry of the region over which the unknown is being expanded. Examples of such element geometries are dipole, square patch, circular patch, cross, and Jerusalem cross, for which the entire domain functions have been successfully applied [3], [13]–[17], [32]. Circular rings and square loops are also studied extensively [33]–[37]. These element geometries are illustrated in Fig. 5.

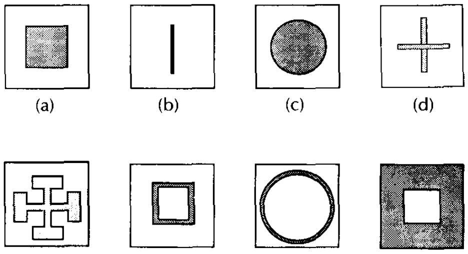
(a) (b) (c) (d)
(e) (f) (g) (h)

Fig. 5. Some typical FSS unit cell geometries. (a) Square patch. (b) Dipole. (c) Circular patch. (d) Cross dipole. (e) Jerusalem cross. (f) Square loop. (g) Circular loop. (h) Square aperture.

The most important advantage of using the entire domain type of basis functions is that the size of the resulting moment method matrix is usually much smaller than that for the subdomain functions; thus, it becomes possible to solve problems for electrically large structures which could not otherwise be handled using subdomain functions. However, for an arbitrary patch or aperture geometries, suitable entire domain basis functions are not available in general. Furthermore, when the impedance loading on the conducting surface is not uniform, the entire domain basis functions that once proved useful for the perfectly conducting FSS are no longer suitable. Thus, for treating FSS screens comprised of arbitrarily-shaped apertures or patches, and for screens with finite conductivities, subdomain basis functions have been found to be more versatile than the entire domain functions [38]–[41], albeit at an increased cost in computer time.

We proceed now to discuss two approaches to solving the operator equation for the induced current (or aperture field) distribution on the screen. Although the basic methodology for solving these equations is the same whether the entire domain or subdomain basis functions are employed to reduce the operator equation to a matrix equation, it should be noted that the double summation appearing in the operator equation, e.g., (11), is carried out differently for these basis functions.

Consider the entire domain basis functions first. To convert the operator equation (11) into a matrix equation, we apply the Galerkin method [3], [30], i.e., choose the testing functions to be the same as the basis functions. Using a suitable set of basis and testing functions in (15) we obtain the following matrix equation for the unknown coefficients C_j

$$\begin{bmatrix} \int J_{xi}^{*} E_x^i \, ds \\ \int J_{yi}^{*} E_y^i \, ds \end{bmatrix} = \sum_j \sum_m \sum_n \begin{bmatrix} \tilde{J}_{xi}^{*} & 0 \\ 0 & \tilde{J}_{yi}^{*} \end{bmatrix} \begin{bmatrix} \tilde{G}_{xx} & \tilde{G}_{xy} \\ \tilde{G}_{yx} & \tilde{G}_{yy} \end{bmatrix} \cdot \begin{bmatrix} \tilde{J}_{xj}(\alpha_{mn}, \beta_{mn}) & 0 \\ 0 & \tilde{J}_{yj}(\alpha_{mn}, \beta_{mn}) \end{bmatrix} \begin{bmatrix} C_{xj} \\ C_{yj} \end{bmatrix} - Z_s \begin{bmatrix} C_{xj} \int J_{xi}^{*} J_{xj} \, ds \\ C_{yj} \int J_{yi}^{*} J_{yj} \, ds \end{bmatrix}, \quad j = 1, 2, \cdots. \tag{16}$$

The numerical efficiency with which the elements of the matrix in (16) can be computed depends upon the asymptotic behaviors of the transforms of the basis functions which, in turn, determine the number of terms needed for convergence of the doubly infinite summations appearing in the expressions for the matrix elements. For some geometries, e.g., a rectangular patch, the number of terms in the double summation is easily related to the total entire domain basis functions used. The minimum number of terms needed to obtain accurate weighting coefficient Cs in (16) is governed by the so-called 'relative convergence' criterion [42]–[45]. For other geometries, this criterion is not as easily found. After the matrix elements are calculated by a straightforward double summation, the integrals appearing in (16) can be evaluated in the following manner. The integrals on the left-hand side of (16) can be identified as the Fourier transforms of the testing functions evaluated at k_{x0} and k_{y0}. On the other hand, the integral on the right-hand side can be evaluated efficiently using a numerical integration technique such as the Gaussian quadrature.

The choices of entire domain basis functions for some typical FSS geometries are listed below:

1) rectangular aperture or patch

$$E_{xpq}^a(x, y) = \hat{x} \frac{T_p\left(\frac{2}{b}x\right)}{\left[1 - \left(\frac{2}{b}x\right)^2\right]^{1/2}} \sin\left[\frac{q\pi}{d}\left(y + \frac{d}{2}\right)\right] \tag{17}$$

$$E_{yrs}^a(x, y) = \hat{y} \sin\left[\frac{r\pi}{b}\left(x + \frac{b}{2}\right)\right] \frac{T_s\left(\frac{2}{d}y\right)}{\left[1 - \left(\frac{2}{d}y\right)^2\right]^{1/2}} \tag{18}$$

$$J_{xpq}(x, y) = \hat{x} \sin\left[\frac{\pi}{b}\left(x + \frac{b}{2}\right)\right] \frac{T_p\left(\frac{2}{d}y\right)}{\left[1 - \left(\frac{2}{d}y\right)^2\right]^{1/2}} \tag{19}$$

and

$$J_{yrs}(x, y) = \hat{y} \frac{T_s\left(\frac{2}{b}x\right)}{\left[1 - \left(\frac{2}{b}x\right)^2\right]^{1/2}} \sin\left[\frac{r\pi}{d}\left(y + \frac{d}{2}\right)\right] \tag{20}$$

where $p, s = 0, 1, \cdots, q, r = 1, 2, \cdots$, and T_i is the ith order Chebyshev function of the first kind.

2) circular aperture or patch

$$E_{\rho pq}(\rho, \phi) = \hat{\rho} \frac{T_p\left(\frac{2}{d}\rho\right)}{\left[1 - \left(\frac{2}{d}\rho\right)^2\right]^{1/2}} e^{jq\phi} \tag{21}$$

$$E_{\phi rs}(\rho, \phi) = \hat{\phi} \left[1 - \left(\frac{2}{d}\rho\right)^2\right]^{1/2} U_r\left(\frac{2}{d}\rho\right) e^{js\phi} \tag{22}$$

$$J_{\rho rs}(\rho, \phi) = \hat{\rho} \left[1 - \left(\frac{2}{d}\rho\right)^2\right]^{1/2} U_r\left(\frac{2}{d}\rho\right) e^{js\phi} \tag{23}$$

$$J_{\phi pq}(\rho, \phi) = \hat{\phi} \frac{T_p\left(\frac{2}{d}\rho\right)}{\left[1 - \left(\frac{2}{d}\rho\right)^2\right]^{1/2}} e^{jq\phi} \tag{24}$$

where $p = 0, 1, 2, \cdots, r = 1, 2, 3, \cdots, q, s = 0, \pm 1, \pm 2, \cdots$, and U_r is the rth order Chebyshev function of the second kind.

3) thin dipole or slot

$$J_{yp} = \hat{y} \sin\left[\frac{p\pi}{L}\left(y + \frac{L}{2}\right)\right] P_x(0, W)\, P_y(0, L) \tag{25}$$

$$J_x = 0 \tag{26}$$

$$E^a_{yq} = \hat{y} \cos\left[\frac{q\pi}{L}\left(y + \frac{L}{2}\right)\right] P_x(0, W)\, P_y(0, L) \tag{27}$$

$$E^a_x = 0 \tag{28}$$

where $p = 1, 2, \cdots, q = 0, 1, 2, \cdots$, and

$$P_x(x_0, D) = \begin{cases} 1, & |x - x_0| \le \frac{D}{2} \\ 0, & \text{otherwise} \end{cases} \quad \text{and}$$

$$P_y(y_0, D) = \begin{cases} 1, & |y - y_0| \le \frac{D}{2} \\ 0, & \text{otherwise} \end{cases}$$

4) cross dipole or slot

$$\begin{aligned} J_{xp} = \hat{x}\left\{C_{1q} \sin\left[\frac{p\pi}{L}\left(x + \frac{L}{2}\right)\right] + \operatorname{sgn}(x) B \cos\left(\frac{\pi}{L}x\right)\right\} \\ \cdot P_x(0, L)\, P_y(0, W) \end{aligned} \tag{29}$$

$$\begin{aligned} J_{yp} = \hat{y}\left\{C_{2q} \sin\left[\frac{p\pi}{L}\left(y + \frac{L}{2}\right)\right] - \operatorname{sgn}(y) B \cos\left(\frac{\pi}{L}y\right)\right\} \\ \cdot P_x(0, W)\, P_y(0, L) \end{aligned} \tag{30}$$

$$\begin{aligned} E^a_{xq} = \hat{x}\left\{C_{1q} \cos\left[\frac{q\pi}{L}\left(x + \frac{L}{2}\right)\right] + \operatorname{sgn}(x) B \cos\left(\frac{\pi}{L}x\right)\right\} \\ \cdot P_x(0, L)\, P_y(0, W) \end{aligned} \tag{31}$$

$$\begin{aligned} E^a_{yq} = \hat{y}\left\{C_{2q} \cos\left[\frac{q\pi}{L}\left(y + \frac{L}{2}\right)\right] - \operatorname{sgn}(y) B \cos\left(\frac{\pi}{L}y\right)\right\} \\ \cdot P_x(0, W)\, P_y(0, L) \end{aligned} \tag{32}$$

and $p = 1, 2, \cdots$, and $q = 0, 1, 2, \cdots$.

5) Jerusalem cross

x-directed current:

$$\hat{x} \sin\left[\frac{p\pi}{L}\left(x + \frac{L}{2}\right)\right] P_x(0, L)\, P_y(0, W) \tag{33}$$

$$\hat{x} \sin\left[\frac{p\pi}{D}\left(x + \frac{D}{2}\right)\right] P_x(0, D)\, P_y\left(\frac{\pm(L - W)}{2}, W\right) \tag{34}$$

y-directed current:

$$\hat{y} \sin\left[\frac{p\pi}{L}\left(y + \frac{L}{2}\right)\right] P_y(0, L)\, P_x(0, W) \tag{35}$$

$$\hat{y} \sin\left[\frac{p\pi}{D}\left(y + \frac{D}{2}\right)\right] P_y(0, D)\, P_x\left(\frac{\pm(L - W)}{2}, W\right) \tag{36}$$

junction basis function:

$$\begin{aligned} &\hat{x} \operatorname{sgn}(x) \sin\frac{\pi x}{L} P_x(0, L)\, P_y(0, W) + \frac{1}{2}\hat{y} \\ &\quad \cdot \operatorname{sgn}(y) \cos\frac{\pi y}{D} P_x\left(\frac{L - W}{2}, W\right) \\ &\quad \cdot P_y(0, D) - \frac{1}{2}\hat{y} \operatorname{sgn}(y) \cos\frac{\pi y}{D} \\ &\quad \cdot P_x\left(\frac{-L + W}{2}, W\right) P_y(0, D) \end{aligned} \tag{37}$$

$$\begin{aligned} &\hat{y} \operatorname{sgn}(y) \sin\frac{\pi y}{L} P_y(0, L)\, P_x(0, W) + \frac{1}{2} \\ &\quad \cdot \hat{x} \operatorname{sgn}(x) \cos\frac{\pi x}{D} P_y\left(\frac{L - W}{2}, W\right) \\ &\quad \cdot P_x(0, D) - \frac{1}{2}\hat{x} \operatorname{sgn}(x) \cos\frac{\pi x}{D} \\ &\quad \cdot P_y\left(\frac{-L + W}{2}, W\right) P_x(0, D) \end{aligned} \tag{38}$$

$$\begin{aligned} &\hat{x} \sin\frac{\pi x}{L} P_x(0, L)\, P_y(0, W) + \frac{1}{2}\hat{y} \operatorname{sgn}(y) \\ &\quad \cdot \cos\frac{\pi y}{D} P_x\left(\frac{L - W}{2}, W\right) P_y(0, D) \\ &\quad + \frac{1}{2}\hat{y} \operatorname{sgn}(y) \cos\frac{\pi y}{D} P_x\left(\frac{-L + W}{2}, W\right) P_y(0, D) \end{aligned} \tag{39}$$

$$\begin{aligned} &\hat{y} \sin\frac{\pi y}{L} P_y(0, L)\, P_x(0, W) + \frac{1}{2}\hat{x} \operatorname{sgn}(x) \\ &\quad \cdot \cos\frac{\pi x}{D} P_y\left(\frac{L - W}{2}, W\right) P_x(0, D) \\ &\quad + \frac{1}{2}\hat{x} \operatorname{sgn}(x) \cos\frac{\pi x}{D} P_y\left(\frac{-L + W}{2}, W\right) P_x(0, D) \end{aligned} \tag{40}$$

$$\begin{aligned} &\hat{x} \operatorname{sgn}(x) \cos\frac{\pi x}{L} P_x(0, L)\, P_y(0, D) - \hat{y} \operatorname{sgn}(y) \\ &\quad \cdot \cos\frac{\pi y}{L} P_x(0, W)\, P_y(0, L). \end{aligned} \tag{41}$$

Typically, the matrix size associated with (16) is on the order of 20 × 20 (or less) when the entire domain basis functions are employed. In contrast, the number of subdomain basis functions required to accurately represent the current or the aperture field is often larger by an order of magnitude. Moreover, the Fourier transforms of the subdomain basis functions do not decay very rapidly until m and n are quite large in α_{mn} and β_{mn}; hence, more Floquet harmonic terms are needed for the double summation to converge. However, as described below, it is possible to accelerate the summation by using the fast Fourier transform algorithm (FFT). If one finds that the matrix size in (16) becomes prohibitively large for subdomain functions and it becomes impractical to use conventional elimination schemes to solve the matrix equation, one may be forced to resort to iterative techniques instead for this purpose.

One of the most frequently used subdomain basis functions is the roof-top [38], [39], which has a triangular or piecewise-linear dependence in the direction of the current and a pulse or stepwise-constant dependence in the orthogonal direction, as shown in Fig. 6. It is expedient to discretize the unit cell into an $N \times N$ grid and to employ equal size roof-top basis functions. Such a discretization scheme that allows the use of the FFT to carry out the double summation appears in the operator equation efficiently. Details of this summing procedure will be given shortly.

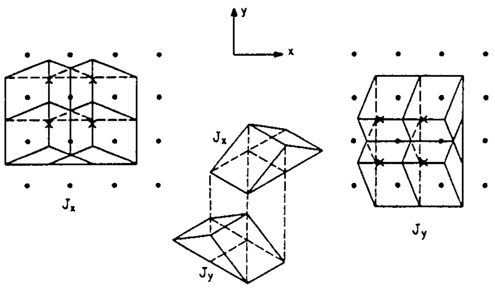

Fig. 6. Rooftop basis functions used to represent current.

Let us direct our attention to the more general problem of solving for the current density distribution, which appears as the unknown in (16). The representations for J_x and J_y take the form

$$J_x = \sum_{-N/2}^{N/2-1} \sum_{-N/2}^{N/2-1} I_x(m, n)\, B_x(m, n) \tag{42}$$

$$J_y = \sum_{-N/2}^{N/2-1} \sum_{-N/2}^{N/2-1} I_y(m, n)\, B_y(m, n) \tag{43}$$

where B_x and B_y are the subdomain basis functions and I_x and I_y are the unknown amplitudes of the current elements corresponding to the subsections that reside within the conducting or resistive surface. It is evident that the element weights for the subdomains that fall outside of the patches are to be set identically equal to zero.

The current basis functions are described by the following equations:

$$B_x(m, n) = \Lambda(m + \tfrac{1}{2})\, \Pi(n) \tag{44}$$

$$B_y(m, n) = \Lambda(m)\, \Pi(n + \tfrac{1}{2}) \tag{45}$$

where for the roof-top discretization, one has

$$\Pi(n) = \begin{cases} 1, & |y - n\Delta y| < \dfrac{\Delta y}{2} \\ 0, & \text{elsewhere} \end{cases} \tag{46}$$

$$\Lambda(m) = \begin{cases} 1 - \dfrac{|x - m\Delta x|}{\Delta x}, & |x - m\Delta x| < \Delta x \\ 0, & \text{elsewhere} \end{cases} \tag{47}$$

where $dx = tx/N$ and $dy = ty/N$. For details of the discretization procedure, the reader is referred to [38]–[40], [46].

Denoting the testing and basis functions in (16) as T and B, the resulting operator equation can be rewritten, after rearranging the order of summations, as follows:

$$-\begin{bmatrix} E_{x0}\tilde{T}_x^*(0, 0)\, P^*(m + \frac{1}{2}, n) \\ E_{y0}\tilde{T}_y^*(0, 0)\, P^*(m, n + \frac{1}{2}) \end{bmatrix} = \left[\sum_{-N/2}^{N/2-1} \sum_{-N/2}^{N/2-1} \begin{bmatrix} \tilde{G}_{xx}(p, q) & \tilde{G}_{xy}(p, q) \\ \tilde{G}_{yx}(p, q) & \tilde{G}_{yy}(p, q) \end{bmatrix} \cdot e^{-j[(k_{xp}p - k_{xm}m)\Delta x + (k_{yq}q - k_{yn}n)\Delta y]} \right] \begin{bmatrix} I_x(m, n) \\ T_y(m, n) \end{bmatrix} \tag{48}$$

with

$$P(m, n) = e^{-j(k_{xi}m\Delta x + k_{yi}n\Delta y)}$$

or

$$-\begin{bmatrix} E_{x0}\tilde{T}_x^*(0, 0)\, P^*(m + \frac{1}{2}, n) \\ E_{y0}\tilde{T}_y^*(0, 0)\, P^*(m, n + \frac{1}{2}) \end{bmatrix} = \left\{ \sum_{-N/2}^{N/2-1} \sum_{-N/2}^{N/2-1} \begin{bmatrix} \tilde{G}_{xx}(m, n) & \tilde{G}_{xy}(m, n) \\ \tilde{G}_{yx}(m, n) & \tilde{G}_{yy}(m, n) \end{bmatrix} \cdot \left\{ \sum_{-N/2}^{N/2-1} \sum_{-N/2}^{N/2-1} e^{-j(k_{sn}n\Delta x + k_{vm}m\Delta y)} \begin{bmatrix} I_x(m, n) \\ I_y(m, n) \end{bmatrix} \right\} \cdot e^{j(k_{sn}n\Delta x + k_{vm}m\Delta y)} \right\} + R_s \begin{bmatrix} F_x(m, n) & 0 \\ 0 & F_y(m, n) \end{bmatrix} \cdot \begin{bmatrix} I_x(m, n) \\ I_y(m, n) \end{bmatrix}. \tag{49}$$

$$-\begin{bmatrix} E_{x0}\tilde{T}_x^*(0, 0)\, P^*(m + \frac{1}{2}, n) \\ E_{y0}\tilde{T}_y^*(0, 0)\, P^*(m, n + \frac{1}{2}) \end{bmatrix} = \begin{bmatrix} P^*(m, n) & 0 \\ 0 & P^*(m, n) \end{bmatrix} \mathrm{FFT}^{-1} \left\{ \begin{bmatrix} \tilde{G}_{xx}(m, n) & \tilde{G}_{xy}(m, n) \\ \tilde{G}_{yx}(m, n) & \tilde{G}_{yy}(m, n) \end{bmatrix} \cdot \left\{ \mathrm{FFT} \left\{ \begin{bmatrix} P(m, n) & 0 \\ 0 & P(m, n) \end{bmatrix} \begin{bmatrix} I_x(m, n) \\ I_y(m, n) \end{bmatrix} \right\} \right\} \right\} + R_s \begin{bmatrix} F_x(m, n) & 0 \\ 0 & F_y(m, n) \end{bmatrix} \begin{bmatrix} I_x(m, n) \\ I_y(m, n) \end{bmatrix} \tag{50}$$

where

$$\tilde{G}'_{xx}(m, n) = \frac{1}{N^2} \sum_{r=-\infty}^{\infty} \sum_{s=-\infty}^{\infty} \tilde{G}_{xx}(m', n')\, \tilde{B}_x(m', n')\, \tilde{T}_x^*(m', n') \tag{51}$$

$$\tilde{G}'_{xy}(m, n) = \frac{1}{N^2} \sum_{r=-\infty}^{\infty} \sum_{s=-\infty}^{\infty} \tilde{G}_{xy}(m', n')\, \tilde{B}_y(m', n')\, \tilde{T}_x^*(m', n') \cdot e^{j(k_{xm'}(\Delta x/2) - k_{yn'}(\Delta y/2))} \tag{52}$$

$$\tilde{G}'_{yx}(m, n) = \frac{1}{N^2} \sum_{r=-\infty}^{\infty} \sum_{s=-\infty}^{\infty} \tilde{G}_{yx}(m', n')\, \tilde{B}_x(m', n')\, \tilde{T}_y^*(m', n') \cdot e^{-j(k_{xm'}(\Delta x/2) - k_{yn'}(\Delta y/2))} \tag{53}$$

$$\tilde{G}'_{yy}(m, n) = \frac{1}{N^2} \sum_{r=-\infty}^{\infty} \sum_{s=-\infty}^{\infty} \tilde{G}_{yy}(m', n')\, \tilde{B}_y(m', n')\, \tilde{T}_y^*(m', n') \tag{54}$$

$\tilde{B}$ and $\tilde{T}$ are the Fourier transforms of the basis and testing functions, respectively. The asterisk represents the complex conjugate operation. E_{x0} and E_{y0} are the magnitudes of the x and y components of the incident field, respectively. When an $N \times N$ FFT is used, $n' = n + rN$ and $m' = m + sN$; $-N/2 \le n, m \le N/2 - 1$. The resistance terms Fs which appear in (48) and (50) will be defined shortly.

The unknown weight coefficients can be obtained either by a direct solution of the matrix equation or by using an iterative procedure, e.g., the conjugate gradient method (CGM) [47], [48]. One distinct difference between the numerical implementation of the direct matrix method and the iterative procedure lies in the manner in which the double summation is evaluated in these two schemes. In the conventional direct matrix method [39], each matrix element is a double summation with the index ranging from $-N_N$ to N_N, and the computation of these double summations is typically very time-consuming. A more efficient way to evaluate the matrix elements is to first compute the double summations in (51) to (54), and then carry out the double summations in (48) via the use of the FFT. When the matrix size becomes prohibitively large, (50) is cast in the form suitable for applying the iterative procedure based upon the conjugate gradient method (CGM).

V. FOURIER TRANSFORM OF THE BASIS AND TESTING FUNCTIONS

The rate of convergence of the iteration algorithm based on CGM depends on the condition number of the operator [49]—the higher the condition number the slower the convergence. The choice of the basis and testing functions plays an important role in determining the condition number [41]. In this paper, we consider two different testing functions, viz., the roof-top and the razor-blade functions, and compare the convergence of the iterative procedures for these two choices. The razor-blade function is defined as follows:

$$T_x(m, n) = \begin{Bmatrix} 1, & |x - m\Delta x| \le \dfrac{\Delta x}{2} \text{ and } y - n\Delta y = 0 \\ 0, & \text{elsewhere} \end{Bmatrix}. \tag{55}$$

The Fourier transforms of the two testing functions are

rooftop

$$\tilde{T}_x(m, n) = \left[\frac{\sin\left(\dfrac{k_{xm}\Delta x}{2}\right)}{\dfrac{k_{xm}\Delta x}{2}} \right]^2 \frac{\sin\left(\dfrac{k_{yn}\Delta y}{2}\right)}{\dfrac{k_{yn}\Delta y}{2}} \tag{56}$$

$$\tilde{T}_y(m, n) = \frac{\sin\left(\dfrac{k_{xm}\Delta x}{2}\right)}{\dfrac{k_{xm}\Delta x}{2}} \left[\frac{\sin\left(\dfrac{k_{yn}\Delta y}{2}\right)}{\dfrac{k_{yn}\Delta y}{2}} \right]^2 \tag{57}$$

razor blade

$$\tilde{T}_x(m, n) = \frac{\sin\left(\dfrac{k_{mx}\Delta x}{2}\right)}{\dfrac{k_{mx}\Delta x}{2}} \tag{58}$$

$$\tilde{T}_y(m, n) = \frac{\sin\left(\dfrac{k_{ny}\Delta y}{2}\right)}{\dfrac{k_{ny}\Delta y}{2}}. \tag{59}$$

Substituting these basis and testing functions in (51) to (54), one can obtain the relationship between the scattered field and the unknown weighting coefficient, either in a matrix form as shown in (48), or in an operator form as in (50). Unlike the scattered field terms, the surface resistance terms, Fs, in (49) and (50) consist of simple multiplication operations instead of convolutions. Each of these resistance terms Fs is the scalar product of the basis and testing functions which can be carried out analytically. The resistance functions F_x and F_y in (49) and (50) are given by

$$F_x(m, n) = C_1\delta(m - 1, n) + C_2\delta(m, n) + C_1(m + 1, n) \tag{60}$$

$$F_y(m, n) = D_1\delta(m, n - 1) + D_2\delta(m, n) + D_1(m, n + 1) \tag{61}$$

where the Kronecker d function is defined as

$$\delta(m, n) = \begin{Bmatrix} 1 & \text{when } m = r \text{ and } n = s \\ 0 & \text{elsewhere} \end{Bmatrix} \tag{62}$$

and s and r are the indices of the current elements $I(s, r)$ in (42) and (43). In addition, some modifications are necessary for the edge element for which $m = -N/2$ or $N/2 - 1$, and $n = -N/2$ or $N/2 - 1$. The δ functions in (60) and (61) are to be modified as follows:

$$m = -\frac{N}{2} \qquad \delta(m - 1, n) \rightarrow e^{jk_{xi}t_x}\delta\left(\frac{N}{2} - 1, n\right) \tag{63}$$

$$m = \frac{N}{2} - 1 \quad \delta(m + 1, n) \rightarrow e^{-jk_{xi}t_x}\delta\left(-\frac{N}{2}, n\right) \tag{64}$$

$$n = -\frac{N}{2} \qquad \delta(m, n - 1) \rightarrow e^{jk_{yi}t_y}\delta\left(m, \frac{N}{2} - 1\right) \tag{65}$$

$$n = \frac{N}{2} - 1 \quad \delta(m, n + 1) \rightarrow e^{-jk_{yi}t_y}\delta\left(m, -\frac{N}{2}\right). \tag{66}$$

For roof-top basis and razor-blade testing, one has

$$C_1 = D_1 = \frac{\Delta x \Delta y}{8} \tag{67}$$

$$C_2 = D_2 = \frac{3}{4}\Delta x \Delta y. \tag{68}$$

On the other hand, for the same basis functions but roof-top testing, the Cs and Ds read

$$C_1 = D_1 = \frac{\Delta x \Delta y}{6} \tag{69}$$

$$C_2 = D_2 = \frac{2}{3} \Delta x \Delta y. \tag{70}$$

Next, we consider the problem of truncating the doubly infinite summations in (51) through (54). When the truncation criterion is chosen such that r and s in (51) to (54) are both equal to zero, it is seen that only $N \times N$ Floquet harmonics are retained in the doubly infinite summation when an $N \times N$ FFT is employed. This approximation is used in [29], [50], and [51] and is valid only if the contributions of the remainder of the Floquet harmonics are negligible; however, in most cases, this assumption usually leads to a less accurate solution.

For the razor-blade testing function, the asymptotic behavior of the summand in the infinite summation appears in (51) to (54) and is given by

$$\frac{1}{mn(m^2 + n^2)^{1/2}}. \tag{71}$$

Owing to the asymptotic behavior of the summand, the convergence of the summation is relatively slow. However, for the roof-top testing function, the asymptotic behavior takes the form:

$$\frac{1}{(mn)^2(m^2 + n^2)^{1/2}}. \tag{72}$$

For this choice of testing functions, the series in (51) to (54) converge considerably faster and the number of terms in each of the summations can be reduced by about a factor of two. As will be shown shortly, choosing a testing function with a superior asymptotic behavior not only improves the rate of convergence for the double summation, it also accelerates the convergence of the iteration algorithm as well.

Let us now consider the procedure for solving (50) using the conjugate gradient method, which is briefly outlined in the Appendix. As can be seen from the Appendix, it is necessary in implementing CGM to construct an adjoint operator and define an inner product. Consider the FFT as a matrix operator. The complex conjugate transpose of the FFT operation is simply equal to the inverse FFT operation and vice versa. In view of this, the adjoint operators for (50) can be written as

$$\left\{\begin{bmatrix} P^* & 0 \\ 0 & P^* \end{bmatrix} \mathbf{FFT}^{-1} \begin{bmatrix} \tilde{G}'^*_{xx} & \tilde{G}'^*_{yx} \\ \tilde{G}'^*_{xy} & \tilde{G}'^*_{yy} \end{bmatrix} \mathbf{FFT} \begin{bmatrix} P & 0 \\ 0 & P \end{bmatrix} + R_s^* \begin{bmatrix} F_x & 0 \\ 0 & F_y \end{bmatrix}\right\}. \tag{73}$$

It should be noted from (60) to (70) that the complex conjugate transposes of the resistance matrix operations in (50) involving Fs remain unchanged as shown in (73).

The unknowns of operator equation (50) are the amplitudes of the basis functions; hence, the inner product can be defined as

$$[\mathbf{J}_s, \mathbf{J}_s] = \sum_{-N/2}^{N/2-1} \sum_{-N/2}^{N/2-1} |I_x(m, n)|^2 + |I_y(m, n)|^2. \tag{74}$$

Once the operator and the adjoint operator have been identified for an equation to be solved and the inner product has been defined, one can follow the procedure outlined in the Appendix to determine the unknown amplitudes of the subdomain basis functions in (42) and (43). However, if the number of unknowns is only moderate, one can employ a direct matrix method for matrix solution, usually with a considerable amount of time saving as compared to that for the iterative solution.

After determining the weighting coefficients of the basis functions, the scattered electric field for a free-standing FSS can be found using (4). The transmission and reflection coefficients for each of the incident and scattered modes are found using [30, eqs. (3.86), (3.89)]. The transmission and reflection coefficients of mode mn due to mode kl incident are given by

$$T_{TM} = \frac{j\omega\epsilon_0 E_z^t}{(k_0^2 + \gamma_{mn}^2)} \left[\frac{\gamma_{mn}(k_0^2 + \gamma_{mn}^2)}{\gamma_{kl}(k_0^2 + \gamma_{kl}^2)}\right]^{1/2} N_{TM} \tag{75}$$

$$T_{TE} = \frac{j}{\beta_{mn}} (E_x^s + j\alpha_{mn}\gamma_{mn}E_z^t) \left[\frac{\gamma_{mn}(k_0^2 + \gamma_{mn}^2)}{\gamma_{kl}(k_0^2 + \gamma_{kl}^2)}\right]^{1/2} N_{TE} \tag{76}$$

$$R_{TM} = \frac{j\omega\epsilon_0 E_z^r}{(k_0^2 + \gamma_{mn}^2)} \left[\frac{\gamma_{mn}(k_0^2 + \gamma_{mn}^2)}{\gamma_{kl}(k_0^2 + \gamma_{kl}^2)}\right]^{1/2} N_{TM} \tag{77}$$

$$R_{TE} = \frac{j}{\beta_{mn}} (E_x^{s'} - j\alpha_{mn}\gamma_{mn}E_z^r) \left[\frac{\gamma_{mn}(k_0^2 + \gamma_{mn}^2)}{\gamma_{kl}(k_0^2 + \gamma_{kl}^2)}\right]^{1/2} N_{TE} \tag{78}$$

where

$$E_z^t = j\frac{(\alpha_{mn}E_x^{s'} + \beta_{mn}E_y^{s'})}{\gamma_{mn}}, \qquad E_z^r = -j\frac{(\alpha_{mn}E_x^{s'} + \beta_{mn}E_y^{s'})}{\gamma_{mn}},$$

$$E_x^{s'} = E_x^s, \qquad E_y^{s'} = E_y^s \quad \text{for } E_z^t;$$

$$E_x^{s'} = E_x^s + E_x^i, \qquad E_y^{s'} = E_x^s + E_y^i \quad \text{for } E_z^r.$$

$$N_{TM} = \begin{Bmatrix} 1 & \text{TM incident} \\ \eta_0 & \text{TE incident} \end{Bmatrix}, \qquad N_{TE} = \begin{Bmatrix} 1 & \text{TE incident} \\ \dfrac{1}{\eta_0} & \text{TM incident} \end{Bmatrix}.$$

For an FSS embedded in a dielectric medium, we need to evaluate the scattered field in (76) and (78) at the dielectric and air interfaces. The relations between the scattered field at the dielectric and air interfaces and the current density on the FSS are given by

$$\begin{bmatrix} \tilde{E}_{x1,2} \\ \tilde{E}_{y1,2} \end{bmatrix} = \begin{bmatrix} \tilde{Z}^e_{t_{1,2}} \cos^2\theta + Z^h_{t_{1,2}} \sin^2\theta & (\tilde{Z}^e_{t_{1,2}} - \tilde{Z}^h_{t_{1,2}}) \sin\theta\cos\theta \\ (\tilde{Z}^e_{t_{1,2}} - \tilde{Z}^h_{t_{1,2}}) \sin\theta\cos\theta & \tilde{Z}^e_{t_{1,2}} \sin^2\theta + \tilde{Z}^h_{t_{1,2}} \cos^2\theta \end{bmatrix} \cdot \begin{bmatrix} \tilde{J}_x \\ \tilde{J}_y \end{bmatrix}$$

$$\tilde{Z}^{e,h}_{t_{1,2}} = \tilde{Z}^{e,h} \frac{Y^{e,h}_{1,2}}{Y^{e,h}_{1,2} \cosh \gamma_{1,2}t_{1,2} + Y_0^{e,h} \sinh \gamma_{1,2}t_{1,2}}. \tag{79}$$

Unlike the free-standing case, the transmission and reflection coefficients of an FSS embedded in a dielectric layer depend on the transmitted and reflected fields from the dielectric layer, respectively, with the FSS removed. The transmission and reflection coefficients can be obtained using (75) to (78) with $E^{s'}$ being replaced by

$$E_x^{s'} = E^s_{x_2} + E^t_{x_2}, \qquad E_y^{s'} = E^s_{y_2} + E^t_{y_2} \quad \text{for } E_z^t \tag{80}$$

$$E_x^{s'} = E^s_{x_1} + E^r_{x_1}, \qquad E_y^{s'} = E^s_{y_1} + E^r_{y_1} \quad \text{for } E_z^r \tag{81}$$

where E_1^r and E_2^t are the reflected and transmitted fields at the upper and lower air-dielectric interfaces, respectively. E_1^r and E_2^t can be evaluated as follows:

$$\begin{bmatrix} E_{x_1}^r \\ E_{y_1}^r \end{bmatrix} = \frac{j}{2}\left[\left(1 - \frac{\gamma_1}{\gamma_0}\right)e^{\gamma_1 t_1}R_1 + \left(1 + \frac{\gamma_1}{\gamma_0}\right)e^{-\gamma_1 t_1}R_2\right] \cdot e^{j(\alpha x + \beta y)}\begin{bmatrix} -\beta \\ \alpha \end{bmatrix} \tag{82}$$

$$\begin{bmatrix} E_{x_2}^t \\ E_{y_2}^t \end{bmatrix} = \frac{j}{2}\left[\left(1 + \frac{\gamma_1}{\gamma_2}\right)(R_1 e^{-\gamma_2 t_2} + R_2 e^{\gamma_2 t_2}) + \left(1 - \frac{\gamma_1}{\gamma_2}\right)(R_2 e^{-\gamma_2 t_2} + R_1 e^{\gamma_2 t_2})\right] \cdot e^{j(\alpha x + \beta y)}\begin{bmatrix} -\beta \\ \alpha \end{bmatrix} \text{—TE} \tag{83}$$

$$\begin{bmatrix} E_{x_1}^r \\ E_{y_1}^r \end{bmatrix} = \frac{-\gamma_0}{\omega\epsilon_0}\left[\left(1 - \frac{\bar{\gamma}_1}{\gamma_0}\right)e^{\gamma_1 t_1}R_1 + \left(1 + \frac{\bar{\gamma}_1}{\gamma_0}\right)e^{-\gamma_1 t_1}R_2\right] \cdot e^{j(\alpha x + \beta y)}\begin{bmatrix} \beta \\ \alpha \end{bmatrix} \tag{84}$$

$$\begin{bmatrix} E_{x_2}^t \\ E_{y_2}^t \end{bmatrix} = \frac{-\gamma_0}{\omega\epsilon_0}\left[\left(1 + \frac{\bar{\gamma}_1}{\gamma_2}\right)(R_1 e^{-\gamma_2 t_2} + R_2 e^{\gamma_2 t_2}) + \left(1 - \frac{\bar{\gamma}_1}{\gamma_2}\right)(R_2 e^{-\gamma_2 t_2} + R_1 e^{\gamma_2 t_2})\right] e^{j(\alpha x + \beta y)}\begin{bmatrix} \beta \\ \alpha \end{bmatrix} \text{—TM.} \tag{85}$$

Substituting (82) to (85) into (75) to (78), the transmission and reflection coefficients for the FSS embedded in dielectric layers can be obtained.

VI. Numerical Results

In this section we present some numerical results that illustrate the application of the techniques, discussed above, for computing the scattering charcteristics of FSSs. For the first example, we consider the problem of free-standing arrays of a perfectly conducting Jerusalem-cross patch geometry, with or without four additional cross dipoles. The unit cells of these FSSs are depicted in Fig. 7(a) and (b). Because of the complexity of the geometries, (4) is solved using the roof-top basis functions with Galerkin testing. Since a fine resolution is required to discretize the geometries, a 32 × 32 grid has been used. The number of unknowns required for the geometries of Fig. 7(a) and (b) are 696 and 584, respectively. In view of the large number of unknowns, the CGM method is preferred over the direct inversion method and is employed to solve the problem. Figs. 8 and 9 show the magnitudes and phases of the reflection coefficients for the two structures described in Fig. 7(a) and (b), respectively. When the angle of incidence is close to normal, and the electric field is polarized in the y direction, no significant difference in the results are observed, perhaps because the Jerusalem cross dominates the frequency response characteristics of this type of FSS. It may be of interest to mention that the criterion for terminating the iterative procedure is that the boundary condition error be reduced to 1 percent, and that the number of iterations required to do this is typically between 100 and 220, depending upon the frequency [41].

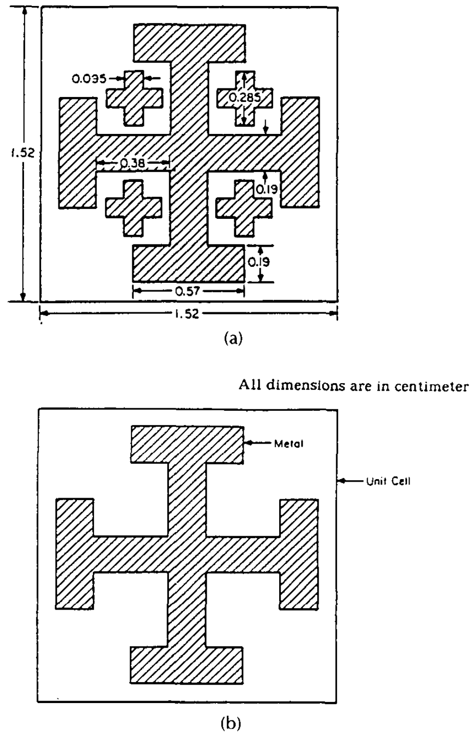

Fig. 7. Unit cells of free-standing arrays of conducting patches of complex geometries. (a) Jerusalem cross with four additional cross dipoles. (b) Jerusalem cross.

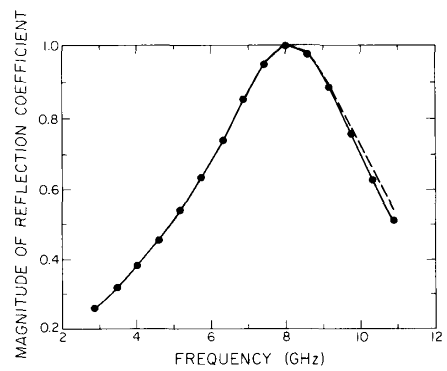

Fig. 8. Magnitude of reflection coefficient versus frequency for the structures shown in Fig. 7(a) and (b). ——— Jerusalem cross with four cross dipoles; - - - - - - Jerusalem cross.

Next, we consider a rectangular slot backed by a thin dielectric sheet as shown in Fig. 10. To analyze this structure, we need to solve for the current density using (7). The composite Green's function can be derived from (8) by setting $\epsilon_{r1} = 1$, and letting t_1 assume any arbitrary value. For normal incidence, the electric field is polarized in the x

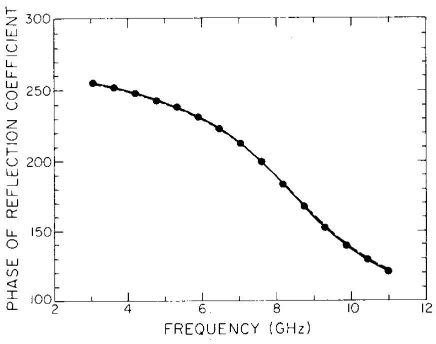

Fig. 9. Phase of reflection coefficient versus frequency for the structures shown in Fig. 7(a) and (b). ——— Jerusalem cross with four cross dipoles; - - - - - - Jerusalem cross.

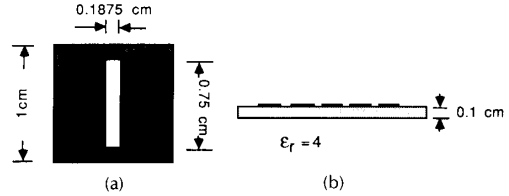

(a) (b)

Fig. 10. Frequency selective surface with dielectric backing. (a) Slot aperture unit cell. (b) A thin dielectric substrate.

direction. As shown in Fig. 11, for $\theta = 1°$, i.e., for the case when the incident angle is very close to normal, the structure resonates at 12.7 GHz. It is found that the structure also resonates at 26.7 GHz and that the bandwidth of this resonance is extremely narrow. As the angle of the incident field increases, the bandwidth of the first resonance increases and the resonance frequency shifts slightly. However, the second resonance, which has a very narrow bandwidth, shifts much closer to the lower resonance as θ increases. It is found that when the direct matrix inverse method is used to solve for the unknown expansion coefficients of either the entire domain or the subdomain basis functions, an abrupt increase in the condition number of the matrix operator is observed as the frequency sweeps through the second resonance that has the narrow bandwidth. As the frequency moves past the resonance, the condition numbers revert back to lower values once again. When the iterative method is used, the abrupt change in the condition number of the operator is reflected in the sudden increase in the number of iterations required to terminate the iteration with the same truncation criterion. In the next example, we will show how this secondary resonance can be eliminated by rearranging the array pattern.

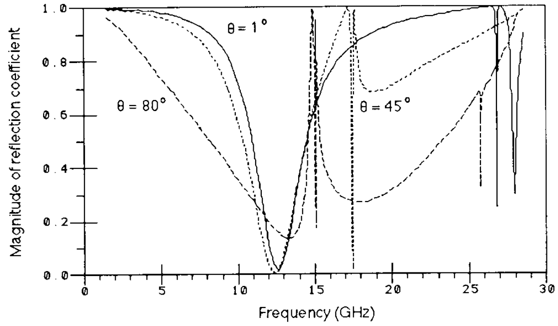

Fig. 11. Frequency response of the FSS depicted in Fig. 10. $\theta = 1°$; TM incidence.

Fig. 12(a) shows an FSS embedded in a stratified dielectric medium, and Fig. 12(b) and (c) show two different array patterns with the same unit cell geometry. The unit cell is a rectangular patch with a sheet resistance of 1 ohm/□. The incident field is polarized in the x direction for normal incidence. As shown by the solid curve in Fig. 13, which corresponds to the array pattern in Fig. 12(b), two secondary resonances occur at about 26 and 28 GHz. When we rearrange the array geometry as in Fig. 12(c), the frequency response of the FSS shifts, as shown in the dotted curve in Fig. 13. It is noted that while the secondary resonances are eliminated, the peak value of the reflection coefficient, the bandwidth, and the resonance frequency are altered only slightly. We also note that owing to the finite losses of the screen, the power reflected by the FSS at resonance is not 100 percent.

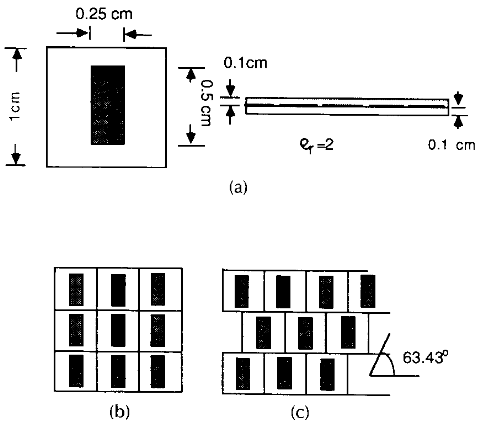

Fig. 12. FSS embedded in a dielectric medium. (a) Rectangular path unit cell. (b) Regular array. (c) Skewed array.

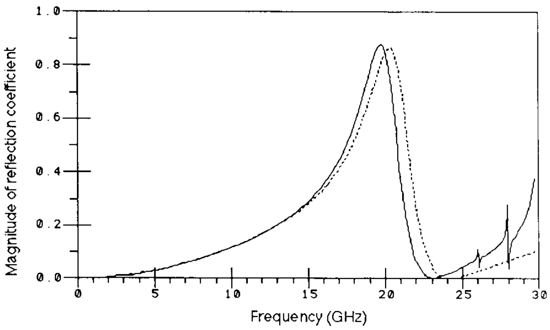

Fig. 13. Frequency response of the FSS dipicted in Fig. 12. $\theta = 1°$; TE incidence.

Having presented a number of illustrative numerical results for the single FSS screen, we next move on to the problem of analyzing multiple screens. This topic is discussed in the next section.

VII. GENERALIZED SCATTERING MATRIX ANALYSIS OF MULTIPLE SCREENS AND SCREENS EMBEDDED IN ONE OR MORE LAYERS OF DIELECTRIC MEDIUM

In this section, we turn to the geometry of multiple screens and develop a methodology based on cascading of scattering matrices for the individual screens. The method is also applicable to the problem of screens embedded in one or more layers of dielectric medium that was discussed earlier in Section IV and [52]–[65]. The material in this section is based primarily on the discussion appearing in [40] and [66]. The general configuration to which the cascade analysis is applicable is shown in Fig. 14.

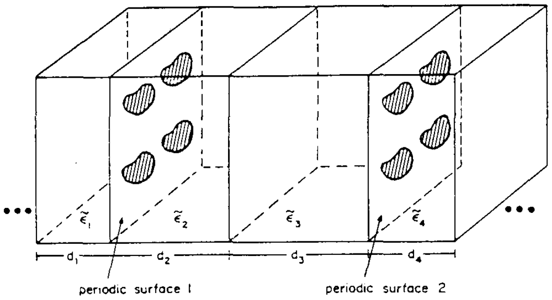

Fig. 14. Diagram of general periodic screen.

A. The Vector Floquet Harmonics

We begin by representing the electric and magnetic fields, which exhibit the periodic behavior in the transverse (to z) direction introduced by the screens, in terms of vector Floquet harmonics weighted by the complex amplitudes $\{a_{pmn}\}$. The representation reads

$$\mathbf{E}(x, y, z) = \sum_{pmn} a^{\pm}_{pmn}[\mathbf{e}_{t_{pmn}}(x, y) + \hat{z}e_{z_{pmn}}(x, y)]e^{\pm jk_{z_{mn}}z} \tag{86a}$$

$$\mathbf{H}(x, y, z) = \sum_{pmn} a^{\pm}_{pmn}[\mathbf{h}_{t_{pmn}}(x, y) + \hat{z}h_{z_{pmn}}(x, y)]e^{\pm jk_{z_{mn}}z} \tag{86b}$$

where the fields are propagating in the $\pm\hat{n}$ direction. The summation is over an infinite number of vector harmonics $\mathbf{e}_{t_{pmn}}$ and $\mathbf{h}_{t_{pmn}}$ ($\infty < m, n < \infty$) and over both polarization states (p = TE and TM). The wave numbers $k_{z_{mn}}$ are given by

$$k_{z_{mn}} = (k^2 - k^2_{x_m} - k^2_{y_n})^{1/2}$$

where k is the propagation constant of the medium. The positive imaginary branch of $k_{z_{mn}}$ is taken when $k^2 < k^2_{x_m} + k^2_{y_n}$. This amplitude sequence $\{a_{pmn}\}$ in (86), which is valid inside the dielectric layer that contains the FSS, serves to characterize the FSS and is used for cascading the screen with other screens or dielectric layers. In (86), $\mathbf{e}_t$ and $\mathbf{h}_t$ are transverse to boundaries with e_z and h_z are the components normal to the boundaries. Let us define the transverse component of the scalar Floquet harmonics [67]

$$\Psi_{mn}(x, y) = \frac{1}{(t_x t_y)^{1/2}} e^{j(k_{x_m}x + k_{y_n}y)} \tag{87}$$

where t_x and t_y are the cell dimensions along x and y, respectively, as the $\hat{z}$ directed potential used in (86). (Note that this formulation is for rectangular geometries; it is easily extended to nonrectangular geometries.) Then the vector harmonics may be expressed as

$$\mathbf{e}_{t_{TE,mn}}(x, y) = -\nabla \times \hat{z}\Psi_{mn}(x, y) \tag{88a}$$

$$\mathbf{h}_{t_{TM,mn}}(x, y) = \nabla \times \hat{z}\Psi_{mn}(x, y) \tag{88b}$$

where the harmonics are divided into those TE and TM to $\hat{z}$. From (87) and (88) we have

$$\mathbf{e}_{t_{TE,mn}}(x, y) = -j(\hat{x}k_{y_n} - \hat{y}k_{x_m})\,\Psi_{mn}(x, y) \tag{89a}$$

$$\mathbf{h}_{t_{TM,mn}}(x, y) = j(\hat{x}k_{y_n} - \hat{y}k_{x_m})\,\Psi_{mn}(x, y). \tag{89b}$$

Because of the plane-wave nature of the vector harmonics, simple relations are found between the electric and magnetic vectors,

$$\hat{n} \times \mathbf{e}_{t_{TE,mn}} = \pm\eta_{TE,mn}\mathbf{h}_{t_{TE,mn}}; \qquad \eta_{TE,mn} = \frac{\omega\mu}{k_{z_{mn}}} \tag{90a}$$

$$\mathbf{h}_{t_{TM,mn}} \times \hat{n} = \pm\frac{1}{\eta_{TM,mn}}\mathbf{e}_{t_{TM,mn}}; \qquad \eta_{TM,mn} = \frac{k_{z_{mn}}}{\omega\epsilon} \tag{90b}$$

where η is the harmonic impedance, and the fields are propagating in the $\pm\hat{n}$ direction. The $\hat{z}$ components are similarly found:

$$h_{z_{TE,mn}}(x, y) = \frac{1}{j\omega\mu}(k^2 - k^2_{z_{mn}})\Psi_{mn}(x, y) \tag{91a}$$

$$e_{z_{TM,mn}}(x, y) = \frac{1}{j\omega\epsilon}(k^2 - k^2_{z_{mn}})\Psi_{mn}(x, y). \tag{91b}$$

The propagation vector also contains the medium propagation constant and angles of incidence, but a simplification results due to Snell's law. The propagation vector components are

$$k_{z_{mn}} = (k^2 - k^2_{x_m} - k^2_{y_n})^{1/2}$$

$$k_{x_m} = \frac{2\pi}{t_x}m + k\sin\theta^i\cos\phi^i$$

$$k_{y_n} = \frac{2\pi}{t_y}n + k\sin\theta^i\sin\phi^i.$$

At a dielectric boundary, the tangential components of the field must be continuous; hence, the phase as given by the tangential components of the propagation vector must also be continuous. For generality, the surface is embedded in a medium identical to that of the lossless originating half space. Therefore, by Snell's law, the product $k\sin\theta^i$ is real and constant throughout the structure, and the angle of incidence θ^i of a harmonic in the originating half-space is identical to the angle of incidence at the periodic surface. If the surface were embedded in a medium different from the originating half-space, the angle of incidence used in the analysis of the periodic surface would have to be initially calculated for the given half-space, thus destroying the generality of the cascade approach. It is also noted that since k_z is a function of the medium propagation constant k, which may be complex, the vector harmonics will propagate with decaying amplitude in a lossy medium.

Many orthogonality relationships may be found for the vector harmonics. One of interest that relates to the calculation of power in the harmonics is

TE harmonics:

$$\int_{\partial s} \mathbf{e}_t \times \boldsymbol{h}_t^* \cdot (\pm\hat{n})\, ds = \frac{1}{\eta^*} \int_{\partial s} \mathbf{e}_t \times (\hat{n} \times \mathbf{e}_t^*) \cdot \hat{n}\, ds$$

$$= \frac{1}{\eta^*} \int_{\partial s} \mathbf{e}_t \cdot \mathbf{e}_t^*\, ds$$

$$= \begin{Bmatrix} \dfrac{1}{\eta^*_{TE,mn}} \|\mathbf{e}_{t_{TE,mn}}\|^2, & m, n = m', n' \\ 0, & m, n \neq m', n' \end{Bmatrix} \tag{92}$$

where the relation between electric and magnetic harmonics (90a) has been used, and nonzero values are obtained for harmonics of similar indices due to the orthogonality of the scalar harmonics. It is noted that since the originating half-space is lossless, i.e., k is real, the tangential components of the propagation vector are real; hence, the vector harmonics are real throughout the dielectric structure, whether or not the dielectric layers are lossy. Because of this, the harmonics are orthogonal as shown above. This orthogonality would be lost if the product $k \sin\theta^i$ of a dielectric layer was imaginary. Similarly, for

TM harmonics:

$$\int_{\partial s} \mathbf{e}_{t_{TM,mn}} \times \boldsymbol{h}^*_{t_{TM,mn}} \cdot (\pm\hat{n})\, ds$$

$$= \begin{Bmatrix} \eta_{TM,mn} \|\boldsymbol{h}_{t_{TM,mn}}\|^2, & m, n = m', n' \\ 0, & m, n \neq m', n' \end{Bmatrix} \tag{93}$$

where the relations between electric and magnetic harmonics ((90b)) have again been used.

B. Normalized Floquet Voltage Waves

Central to the cascade connection of dielectric layers and periodic surfaces is the calculation of the normalized Floquet voltage waves. Extended to the Floquet vector harmonics defined above, these traveling waves are identical to the traveling waves defined for the guided modes used in microwave circuit theory. The normalized voltage waves, with amplitudes given by an element of the sequence $\{a_{pmn}\}$, are sufficient to describe the fields in any terminal plane. These voltages are given by

$$v^{\pm}_{pmn}(z) = a^{\pm}_{pmn} \left[\int_{\partial s} \mathbf{e}_{t_{pmn}} \times \boldsymbol{h}^*_{t_{pmn}} \cdot (\pm\hat{n})\, ds \right]^{1/2} e^{\pm j k_{z_{mn}} z} \tag{94}$$

at a plane z, for fields propagating in the $\pm\hat{n}$ direction. The units are the square root of power [$W^{1/2}$]; hence, the square of these waves may be interpreted as a propagating, evanescent or decaying (power) wave depending upon the propagation constant k_z. The complex amplitude coefficient a_{pmn} has been deliberately left outside the square root in order to preserve the phase of the wave associated with each harmonic.

With the aid of the orthogonality relationship (90), the normalized voltage wave for each harmonic simplifies to

$$V^{\pm}_{TE,mn}(z) = a^{\pm}_{TE,mn} \frac{1}{(\eta^*_{TE,mn})^{1/2}} \|\mathbf{e}_{t_{TE,mn}}\| e^{\pm j k_{z_{mn}}} \tag{95a}$$

$$V^{\pm}_{TM,mn}(z) = a^{\pm}_{TM,mn} (\eta_{TM,mn})^{1/2} \|\boldsymbol{h}_{t_{TM,mn}}\| e^{\pm j k_{z_{mn}}} \tag{95b}$$

where it is noted that

$$\|\mathbf{e}_{t_{TE,mn}}\| = \|\boldsymbol{h}_{t_{TM,mn}}\| = (k^2_{x_m} + k^2_{y_n})^{1/2}. \tag{96}$$

The scattering parameters that will characterize a terminal plane are defined in the usual manner

$$\overline{V}^S = \boldsymbol{S}\overline{V}^I \tag{97}$$

where $\overline{V}^S$ and $\overline{V}^I$ indicate the unknown scattered S and known incident I normalized voltage wave vectors, respectively. Each vector contains all the TE and TM waves outlined above as elements with the appropriate direction of propagation taken for either the incident or scattered wave. With reference to Fig. 15, the vectors at a terminal plane z are

$$\overline{V}^I = \begin{bmatrix} \overline{V}^{I_1} \\ \overline{V}^{I_2} \end{bmatrix} \qquad \overline{V}^S = \begin{bmatrix} \overline{V}^{S_1} \\ \overline{V}^{S_2} \end{bmatrix} \tag{98}$$

with the direction of propagation relative to $\hat{n}$ indicated by the arrows in Fig. 15. Equation (97) then is

$$\begin{bmatrix} \overline{V}^{S_1} \\ \overline{V}^{S_2} \end{bmatrix} = \begin{bmatrix} \boldsymbol{S}_{11} & \boldsymbol{S}_{12} \\ \boldsymbol{S}_{21} & \boldsymbol{S}_{22} \end{bmatrix} \cdot \begin{bmatrix} \overline{V}^{I_1} \\ \overline{V}^{I_2} \end{bmatrix} \tag{99}$$

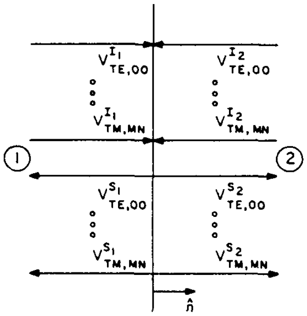

Fig. 15. Terminal plane defining normalized voltage waves.

where $\boldsymbol{S}$ has now been divided into submatrices. In general, each submatrix may be rectangular, i.e., for I incident harmonics, there will be J scattered harmonics resulting in the submatrices having I columns and J rows. This may correspond to a single harmonic incident upon a periodic surface, scattering ideally into an infinite number (but truncated finite number) of harmonics on each side of the surface. Since, in general, each component will be considered as an arbitrary element of the screen where the number of incident and scattered harmonics is not known *a priori*, and since the component may be cascaded with other arbitrary components, the submatrices will be calculated for an equal number of incident and scattered harmonics. The submatrices will be of order $2MN$, (M, N) being the total number of harmonics in the $(\hat{x}, \hat{y})$ directions, with the factor 2 accounting for the TE and TM states. The scattering parameters will now be outlined for the periodic surface and dielectric boundary—the two components used to construct a screen.

C. Generalized Scattering Parameters of Periodic Surfaces and Dielectric Boundaries

The scattering parameters of the first element of a periodic screen (a periodic surface) are found from the Floquet harmonic amplitudes $\{a_{pmn}\}$. The term *generalized* is applied because the parameters are calculated for both propagating and evanescent harmonics [31]. The coefficients $\{a_{pmn}\}$ weight the vector harmonics incident upon and scattered from the surface. When the surface is symmetric, $\boldsymbol{S}_{21} = \boldsymbol{S}_{12} = \boldsymbol{T}$, and because of the reciprocal nature of the surface, $\boldsymbol{S}_{11} = \boldsymbol{S}_{22} = \boldsymbol{R}$. The coupling of an incident harmonic into a forward scattered harmonic, i.e., transmitted harmonic for a surface at some plane z, then is

$$T^{(pmn)_s}_{(pmn)_i}(z) = \frac{V^{S_2}_{(pmn)_s}(z)}{V^{I_1}_{(pmn)_i}(z)}, \tag{100a}$$

while the coupling into a backscattered harmonic, i.e., reflected harmonic is

$$R^{(pmn)_s}_{(pmn)_i}(z) = \frac{V^{S_1}_{(pmn)_s}(z)}{V^{I_1}_{(pmn)_i}(z)} \tag{100b}$$

where the subscript indicates incident harmonics, and the superscript indicates scattered harmonics. Since both TE and TM harmonics may be incident, and since the surface allows coupling of energy from one polarization into another, there will be four transmission and four reflection coefficients associated with each pair of incident and reflected harmonics. The coefficients are explicitly given in Table 1 for a surface in the plane $z = 0$. The total fields are the sum of the incident and scattered fields; hence, the copolarized transmission and reflection coefficients contain the extra weighting coefficient $a^{i}_{TE(mn)_i}\,\delta_{(mn)_i(mn)_s}$, which is the addition of the incident field harmonic to the identical forward scattered harmonic; δ_{ij} is the Kronecker delta function. This additional term does not enter into any other coefficient due to the orthogonality of the harmonics. The scattering parameters may be physically interpreted as the coupling of energy from one harmonic into another, the coupling being directly found from the ratio of harmonic amplitudes modified by the impedance and norm of each harmonic. This modification is necessary because of the differing amounts of power associated with each harmonic.

Table 1 Scattering Parameters of Surface Lying in Plane $z = 0$

Periodic Surface Scattering Parameters
Transmission Scattering Parameters
Copolarized
$T^{TE(mn)_s}_{TE(mn)_i} = \dfrac{a^{+}_{TE(mn)_i}\,\delta_{(mn)_i(mn)_s} + a^{+}_{TE(mn)_s}}{a^{i}_{TE(mn)_i}} \left(\dfrac{\overset{*}{\eta}_{TE(mn)_i}}{\overset{*}{\eta}_{TE(mn)_s}}\right)^{1/2} \dfrac{\Vert \bar{e}_{tTE(mn)_s} \Vert}{\Vert \bar{e}_{tTE(mn)_i} \Vert}$
$T^{TM(mn)_s}_{TM(mn)_i} = \dfrac{a^{+}_{TM(mn)_i}\,\delta_{(mn)_i(mn)_s} + a^{+}_{TM(mn)_s}}{a^{i}_{TM(mn)_i}} \left(\dfrac{\eta_{TM(mn)_s}}{\eta_{TM(mn)_i}}\right)^{1/2} \dfrac{\Vert \bar{h}_{tTM(mn)_s} \Vert}{\Vert \bar{h}_{tTM(mn)_i} \Vert}$
Cross Polarized
$T^{TM(mn)_s}_{TE(mn)_i} = \dfrac{a^{+}_{TM(mn)_s}}{a^{i}_{TE(mn)_i}} (\eta_{TM(mn)_s}\overset{*}{\eta}_{TE(mn)_i})^{1/2} \dfrac{\Vert \bar{h}_{tTM(mn)_s} \Vert}{\Vert \bar{e}_{tTE(mn)_i} \Vert}$
$T^{TE(mn)_s}_{TM(mn)_i} = \dfrac{a^{+}_{TE(mn)_s}}{a^{i}_{TM(mn)_i}} \dfrac{1}{(\eta_{TM(mn)_i}\overset{*}{\eta}_{TE(mn)_s})^{1/2}} \dfrac{\Vert \bar{e}_{tTE(mn)_s} \Vert}{\Vert \bar{h}_{tTM(mn)_i} \Vert}$
Reflection Scattering Parameters
Copolarized
$R^{TE(mn)_s}_{TE(mn)_i} = \dfrac{a^{-}_{TE(mn)_s}}{a^{i}_{TE(mn)_i}} \left(\dfrac{\overset{*}{\eta}_{TE(mn)_i}}{\overset{*}{\eta}_{TE(mn)_s}}\right)^{1/2} \dfrac{\Vert \bar{e}_{tTE(mn)_s} \Vert}{\Vert \bar{e}_{tTE(mn)_i} \Vert}$
$R^{TM(mn)_s}_{TM(mn)_i} = \dfrac{a^{-}_{TM(mn)_s}}{a^{i}_{TM(mn)_i}} \left(\dfrac{\eta_{TM(mn)_s}}{\eta_{TM(mn)_i}}\right)^{1/2} \dfrac{\Vert \bar{h}_{tTM(mn)_s} \Vert}{\Vert \bar{h}_{tTM(mn)_i} \Vert}$
Cross Polarized
$R^{TM(mn)_s}_{TE(mn)_i} = \dfrac{a^{-}_{TM(mn)_s}}{a^{i}_{TE(mn)_i}} (\eta_{TM(mn)_s}\overset{*}{\eta}_{TE(mn)_i})^{1/2} \dfrac{\Vert \bar{h}_{tTM(mn)_s} \Vert}{\Vert \bar{e}_{tTE(mn)_i} \Vert}$
$R^{TE(mn)_s}_{TM(mn)_i} = \dfrac{a^{-}_{TE(mn)_s}}{a^{i}_{TM(mn)_i}} \dfrac{1}{(\eta_{TM(mn)_i}\overset{*}{\eta}_{TE(mn)_s})^{1/2}} \dfrac{\Vert \bar{e}_{tTE(mn)_s} \Vert}{\Vert \bar{h}_{tTM(mn)_i} \Vert}$

The second element of an arbitrary screen is the boundary separating two homogeneous dielectrics. Each harmonic, having the form of a plane wave, will have scattering parameters simply related to the transmission and reflection coefficients of the harmonic, and since there is no coupling between harmonics at the interface, the scattering parameter matrices are diagonal. For a dielectric boundary between media 1 and 2 (see Fig. 15), the scattering matrix is antireciprocal and symmetric, being related to the medium impedances as follows:

$\boldsymbol{S}_{11} = -\boldsymbol{S}_{22} = \boldsymbol{R}$:

$$R^{(pmn)_s}_{(pmn)_i} = \frac{V^{S_1}_{(pmn)_s}(0)}{V^{I_1}_{(pmn)_i}(0)} = \begin{Bmatrix} \dfrac{\eta^{2}_{pmn} - \eta^{1}_{pmn}}{\eta^{2}_{pmn} + \eta^{1}_{pmn}}, & i = s \\ 0, & i \neq s \end{Bmatrix} \tag{101a}$$

$\boldsymbol{S}_{12} = \boldsymbol{S}_{21} = \boldsymbol{T}$:

$$T^{(pmn)_s}_{(pmn)_i} = \frac{V^{S_2}_{(pmn)_s}(0)}{V^{I_1}_{(pmn)_i}(0)} = \begin{Bmatrix} \dfrac{2(\eta^{1}_{pmn}\eta^{2}_{pmn})^{1/2}}{\eta^{2}_{pmn} + \eta^{1}_{pmn}}, & i = s \\ 0, & i \neq s \end{Bmatrix}. \tag{101b}$$

With the scattering parameters of the two elements derived, it only remains to outline the procedure to cascade an arbitrary number of elements to find the composite scattering parameters of a multiple screen embedded in a multilayered dielectric.

D. Cascaded Connection of Generalized Scattering Parameters

The scattering parameters given by Table 1 and (101) define the relationship between the incident and scattered harmonics at a terminal plane. Being a set of linear equations, the manipulations of linear algebra may be directly applied to find the composite scattering parameters of more than one component. The formalism due to Sazonov *et al.* [68] has been used and modified to account for the specific components used (surfaces and dielectric layers).

A schematic illustrating the connection of two components is shown in Fig. 16. The components, being separated by a distance d, are characterized, e.g., by a surface embedded in a medium a distance d away from a dielectric boundary separating a second medium, or, e.g., by two dielectric boundaries separating a dielectric layer of thickness d from neighboring media. The normalized voltage waves to the left of the composite structure are labeled α, to the right γ, and between elements β_1 and β_2, respectively, at the terminal planes of each element. Since the waves between ele-

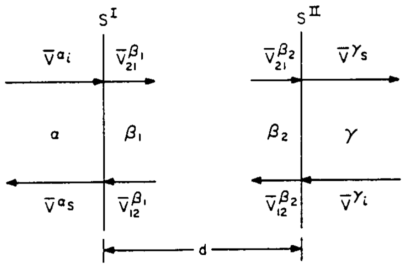

Fig. 16. Schematic showing cascade connection of scattering matrices S^I and S^{II}.

ments are the combination of the incident and scattered waves of each element, the individual incident and scattered waves cannot be isolated; hence, the combination is labeled $\bar{V}^{\beta_{12}}_{12}$ and $\bar{V}^{\beta_{12}}_{21}$, respectively, at each terminal plane.

For the component characterized by $\boldsymbol{S}^I$, the defining equations for the scattered waves due to incident waves are

$$\begin{bmatrix} \bar{V}^{\alpha_s} \\ \bar{V}^{\beta_1}_{21} \end{bmatrix} = \begin{bmatrix} \boldsymbol{S}_{\alpha\alpha} & \boldsymbol{S}_{\alpha\beta_1} \\ \boldsymbol{S}_{\beta_1\alpha} & \boldsymbol{S}_{\beta_1\beta_1} \end{bmatrix} \cdot \begin{bmatrix} \bar{V}^{\alpha_i} \\ \bar{V}^{\beta_1}_{12} \end{bmatrix}, \tag{102}$$

and for the component characterized by $\boldsymbol{S}^{II}$

$$\begin{bmatrix} \bar{V}^{\beta_2}_{12} \\ \bar{V}^{\gamma_s} \end{bmatrix} = \begin{bmatrix} \boldsymbol{S}_{\beta_2\beta_2} & \boldsymbol{S}_{\beta_2\gamma} \\ \boldsymbol{S}_{\gamma\beta_2} & \boldsymbol{S}_{\gamma\gamma} \end{bmatrix} \begin{bmatrix} \bar{V}^{\beta_2}_{21} \\ \bar{V}^{\gamma_i} \end{bmatrix}. \tag{103}$$

Since the normalized voltage waves at terminal planes are traveling waves, the waves at terminal planes are simply related as

$$\bar{V}^{\beta_2}_{21} = \boldsymbol{P}\bar{V}^{\beta_1}_{21} \tag{104a}$$

$$\bar{V}^{\beta_1}_{12} = \boldsymbol{P}\bar{V}^{\beta_2}_{12} \tag{104b}$$

where $\boldsymbol{P}$ is a diagonal propagator matrix, with a diagonal element being $e^{-jk_{z_{mn}}d}$ for each *mn*th harmonic.

The relations between the normalized voltage waves of each component may be combined to produce a composite scattering matrix defined as

$$\begin{bmatrix} \bar{V}^{\alpha_s} \\ \bar{V}^{\gamma_s} \end{bmatrix} = \begin{bmatrix} \boldsymbol{S}^{\Sigma}_{\alpha\alpha} & \boldsymbol{S}^{\Sigma}_{\alpha\gamma} \\ \boldsymbol{S}^{\Sigma}_{\gamma\alpha} & \boldsymbol{S}^{\Sigma}_{\gamma\gamma} \end{bmatrix} \begin{bmatrix} \bar{V}^{\alpha_i} \\ \bar{V}^{\gamma_i} \end{bmatrix} \tag{105}$$

where Σ indicates the scattering matrices characterizing the composite structure. An intermediate step in the matrix combination is the calculation of the internal waves $\bar{V}_{12}$ and $\bar{V}_{21}$. The knowledge of these waves then allows the calculation of fields at any point in between the boundaries. Combining (102) and (103) and using (104a) and (104b) give

$$\begin{bmatrix} \bar{V}^{\beta_1}_{12} \\ \bar{V}^{\beta_2}_{21} \end{bmatrix} = \begin{bmatrix} \boldsymbol{H}_2\boldsymbol{S}_{\beta_2\beta_2}\boldsymbol{P}\boldsymbol{S}_{\beta_1\alpha} & \boldsymbol{H}_2\boldsymbol{S}_{\beta_2\gamma} \\ \boldsymbol{H}_1\boldsymbol{S}_{\beta_1\alpha} & \boldsymbol{H}_1\boldsymbol{S}_{\beta_1\beta_1}\boldsymbol{P}\boldsymbol{S}_{\beta_2\gamma} \end{bmatrix} \begin{bmatrix} \bar{V}^{\alpha_i} \\ \bar{V}^{\gamma_i} \end{bmatrix} \tag{106}$$

where

$$\boldsymbol{H}_1 = (\boldsymbol{P}^{-1} - \boldsymbol{S}_{\beta_1\beta_1}\boldsymbol{P}\boldsymbol{S}_{\beta_2\beta_2})^{-1}$$

$$\boldsymbol{H}_2 = (\boldsymbol{P}^{-1} - \boldsymbol{S}_{\beta_2\beta_2}\boldsymbol{P}\boldsymbol{S}_{\beta_1\beta_1})^{-1}.$$

Completing the matrix manipulations to find the composite scattering parameters results in

$$\boldsymbol{S}^{\Sigma}_{\alpha\alpha} = \boldsymbol{S}_{\alpha\alpha} + \boldsymbol{S}_{\alpha\beta_1}\boldsymbol{H}_2\boldsymbol{S}_{\beta_2\beta_2}\boldsymbol{P}\boldsymbol{S}_{\beta_1\alpha} \tag{107a}$$

$$\boldsymbol{S}^{\Sigma}_{\alpha\gamma} = \boldsymbol{S}_{\alpha\beta_1}\boldsymbol{H}_2\boldsymbol{S}_{\beta_2\gamma} \tag{107b}$$

$$\boldsymbol{S}^{\Sigma}_{\gamma\alpha} = \boldsymbol{S}_{\alpha\beta_2}\boldsymbol{H}_1\boldsymbol{S}_{\beta_2\alpha} \tag{107c}$$

$$\boldsymbol{S}^{\Sigma}_{\gamma\gamma} = \boldsymbol{S}_{\gamma\gamma} + \boldsymbol{S}_{\gamma\beta_2}\boldsymbol{H}_1\boldsymbol{S}_{\beta_1\beta_1}\boldsymbol{P}\boldsymbol{S}_{\beta_2\gamma}. \tag{107d}$$

The resultant scattering matrices now characterize the composite structure, and, as in the individual parameters, are a function of frequency. A multicomponent screen may be built by repeating the above procedure, using the composite scattering parameters of the initial two components of the screen as the first scattering parameter matrix, with the scattering parameters of the next component being the second matrix. By repeatedly adding components in this fashion, a general screen is constructed from individual components with the layering being arbitrary.

The composite scattering parameters may also be found by other means. An alternative formulation involves the use of the *T* or transfer parameters. In this approach, the scattering parameters are first transformed to transfer parameters; the transfer parameters of many layers, or for multiple screens, are cascaded to find a composite transfer matrix; the composite matrix is then transformed back to a scattering matrix. A nearly equal number of matrix manipulations are involved in each approach, and the final scattering parameters calculated are identical. The direct approach outlined here is somewhat preferable, however, because the *T*-Matrix approach is sometimes numerically unstable. In addition, the procedure outlined here lends physical insight into the analysis, and leads to an expression for the composite scattering parameter that can be easily interpreted. This may be seen by considering an example where two elements are separated by a distance such that only a single harmonic interacts between them, and there is no coupling between TE and TM harmonics. This could correspond to a periodic surface with rectangular patches which is displaced from a dielectric layer by an appreciable fraction of a wavelength. The composite reflection coefficient of the structure is given by (107a) and for the single propagating harmonic, reduces to

$$R^{\Sigma} = R_{\alpha\alpha} + T_{\alpha\beta_1}R_{\beta_2\beta_2}T_{\beta_1\alpha}\frac{e^{-jk_7d}}{1 - R_{\beta_2\beta_2}R_{\beta_1\beta_1}e^{-j2k_zd}} \tag{108}$$

where *R* and *T* have been used as the reflection and transmission coefficients of the propagating harmonic within each matrix $\boldsymbol{S}$. Fig. 17 diagrams the structure, showing the

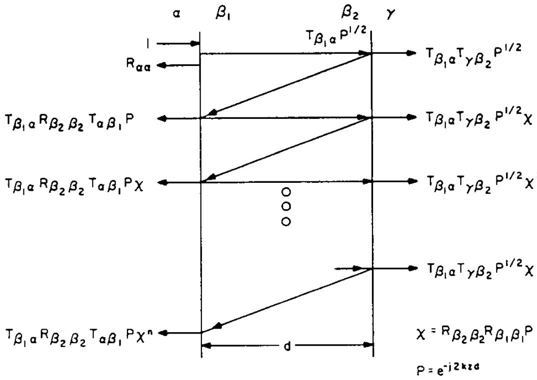

Fig. 17. Schematic showing multiple reflections of voltage waves within a dielectric layer.

wave suffering multiple reflections within the region between dielectric boundaries and reflecting and transmitting fractional amounts of the incident wave upon each reflection. From this picture of the interactions, the composite reflection coefficient may be derived, and when allowed to be generalized to all harmonics, whether propagating or evanescent, the matrix reflection scattering parameters can be obtained. For the single harmonic pictured, summing the reflected waves gives

$$R^{\Sigma} = R_{\alpha\alpha} + T_{\alpha\beta_1}R_{\beta_2\beta_2}T_{\beta_1\alpha}e^{-j2k_zd}(1 + \chi + \chi^2 + \cdots + \chi^n) \tag{109}$$

where

$$\chi = R_{\beta_2\beta_2}R_{\beta_1\beta_1}e^{-j2k_zd}$$

In the limit of all reflections,

$$\lim_{n \to \infty} R^{\Sigma} = R_{\alpha\alpha} + T_{\alpha\beta_1}R_{\beta_2\beta_2}T_{\beta_1\alpha}\frac{e^{-j2k_zd}}{1 - R_{\beta_2\beta_2}R_{\beta_1\beta_1}e^{-j2k_zd}}, \tag{110}$$

which is the reflection coefficient found using the cascade analysis. The same analysis holds for the composite transmission coefficient. Additional layers may be added, but a physical picture quickly becomes muddled.

By examining the composite scattering matrices as given by (107d), the relations between individual and composite scattering parameters may also be easily seen. For example, from the composite reflection matrix

$$S^{\Sigma}_{\alpha\alpha} = S_{\alpha\alpha} + S_{\alpha\beta_1}HS_{\beta_2\beta_2}PS_{\beta_1\alpha},$$

it is observed that if the second component allows no reflection ($S_{\beta_2\beta_2} = 0$), the composite reflected waves will simply be those of the first component and hence not be altered by the second component. By examining individual harmonics, it is observed that if the second component allows no reflection into the (0, 0) harmonic, and also if the (0, 0) harmonic reflects no energy into any other harmonic (corresponding to a zero row and column for each polarization in $S_{\beta_2\beta_2}$), then similarly, the composite reflected (0, 0) harmonic will only be that of the first component. A similar reasoning follows for the transmission parameters and may be extended to multiple components. This line of reasoning adds insight into the cascade formulation and can be beneficial when attempting to cascade arbitrary elements to produce a desired characteristic response.

E. Accuracy of the Cascade Connection

Because both propagating and higher-order harmonics carry energy, the accuracy of either the resonant wavelength of the structure or power dissipated in the dielectric as outlined in the previous sections will depend upon the amplitude of truncated harmonics. The resonant wavelength is affected by harmonics interacting with dielectric interfaces. The strongest interaction—that at the surface dielectric interface—can be isolated by backing the periodic surface with a dielectric half-space. In the cascade analysis, a gap of infinitesimal thickness is inserted between the surface and dielectric and allowed to shrink to zero. In the limit, an infinite number of harmonics would ideally be necessary to characterize the interface. (As previously noted, the total field at any plane is represented by the Floquet voltage waves; hence, a complete description of the fields would require an infinite superposition of those waves.) The accuracy of the characterization is then dependent on the interaction of higher-order harmonics and their amplitudes decay relatively slowly for large ϵ_r. The composite Green's function approach described in Section IV is better-suited for handling the large ϵ_r case.

In order to illustrate the application of the cascade approach, we consider a rectangular array of crossed dipoles as shown in the inset of Fig. 18. Exciting the structure is normally incident plane wave with a $\hat{y}$-directed electric field. The number of harmonics summed will be 2, 10, 18, 26, or 42, which are the numbers (TE and TM) contained within concentric circles on the reciprocal lattice of the surface. The resonant wavelength of the structure is plotted in Fig. 18 for a dielectric half-space of $\epsilon_r = 2.0$. The result shows little change in the resonant wavelength when more than 18 harmonics are summed. However, as pointed out earlier, this number can increase substantially for larger ϵ_r.

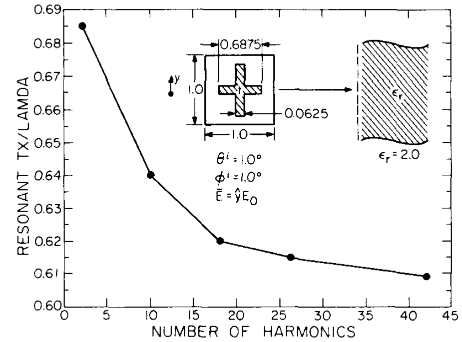

Fig. 18. Harmonic convergence of the resonant wavelengths.

Both the accuracy of the power dissipated at any point and the interaction of higher-order harmonics with dielectric-dielectric interfaces can be ascertained from the amplitude of the harmonics as they propagate or decay with distance. Writing the normalized voltage wave (94) as

$$V_r(z) = a'_r e^{-jk_{z_r}z} \tag{111}$$

where r indicates the subscripts pmn included with the rth concentric ring of the reciprocal lattice, and the prime indicates that the normalization integral of (94) is included in a'_r. Normalizing the voltage wave in ring r to the (single) propagating (TE) harmonic in ring 1 gives

$$\ln\left|\frac{V_r(z)}{V_1(0)}\right| = -k_{z_r}|z| + \ln\left|\frac{a'_r}{a'_1}\right|, \tag{112}$$

the equation of a straight line. The slope is simply the negative of the attenuation constant (for the evanescent harmonics) with the intercept the numerically found complex amplitude. Equation (112) is plotted in Fig. 19 with the distance z in units of wavelength in the dielectric. The cell size (t_x/λ) is 0.57 where nearly 70-percent of the power is transmitted into the dielectric. It is seen that a distance of 0.25 λ_d, amplitudes of the voltage waves in the fourth ring have decayed to nearly 0.01 percent of the propagating wave.

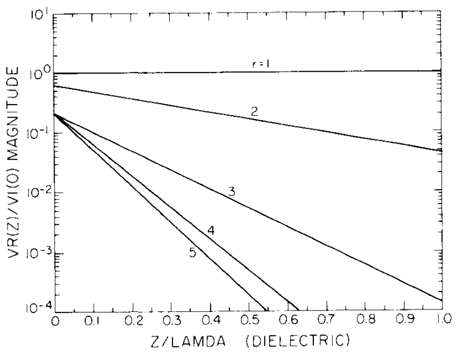

Fig. 19. Decay of harmonics with distance within the dielectric.

F. Numerical Results for Typical Cascaded Geometries

Because the combination of surface geometries, dielectric layers, and number of cascaded surfaces may be quite large, only the results for typical geometries showing the effects of dielectric layering and lossy layers will be presented in this paper. The effect of dielectric backing of varying thicknesses on the crossed-dipole surface of the inset of Fig. 18 is shown in Fig. 20. The dimensions now are in centimeters, and the resonant wavelength is plotted versus dielectric thickness for dielectrics of permittivities $\epsilon_r = 2.0$ and 4.0. A total of 18 harmonics was summed (the third ring of the reciprocal lattice). It is seen that as the thickness is increased the resonant wavelength approaches that of a half-space, with a permittivity of $\epsilon_r = 4.0$ having a greater effect on the resonant wavelength as compared to that for $\epsilon_r = 2.0$.

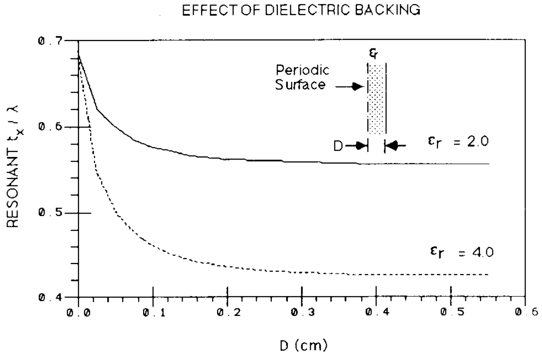

Fig. 20. Effect of dielectric backing on periodic screen of Fig. 18.

The magnitude of the power reflection coefficient versus cell size is plotted in Fig. 21 for the same crossed-dipole surface backed with a 0.3-cm-thick dielectric layer. Shown are curves for permittivities 2.0 and 4.0 compared to a free-standing surface ($d = 0$). The resonant wavelength shifts to lower wavelengths, with the resonant bandwidth generally decreasing as the permittivity is increased.

A lossy structure is considered in Fig. 22. The structure consists of a crossed-slot aperture backed by a lossy dielectric layer of permittivity $\epsilon_r = 3 - j4$ (see insert of Fig. 22(a)). Because of the high loss in the layer, no power is transmitted through the structure, all energy being reflected or dissipated within the layer. Plotted are the reflected power and the fraction of total power dissipated in the dielectric layer as a function of the cell size. For comparison, the magnitude of the power reflection coefficient of the free-standing surface is shown (dotted line). The sharp null of the free-standing surface is removed when the lossy layer is added with a minimum in the reflection coefficient occurring near $t_x/\lambda = 0.9$. Fig. 22(b) is a contour plot of the dissipated power volume density normalized to the total incident power at a plane 0.1 cm into the dielectric. The excitation wavelength is $t_x/\lambda = 0.9$; the labels are scaled by 10 000 and the crossed

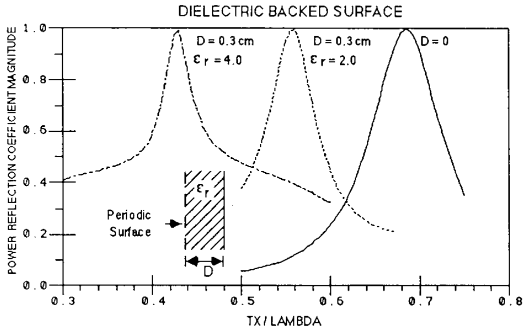

Fig. 21. Spectral response of the periodic screen of Fig. 18 with dielectric backing.

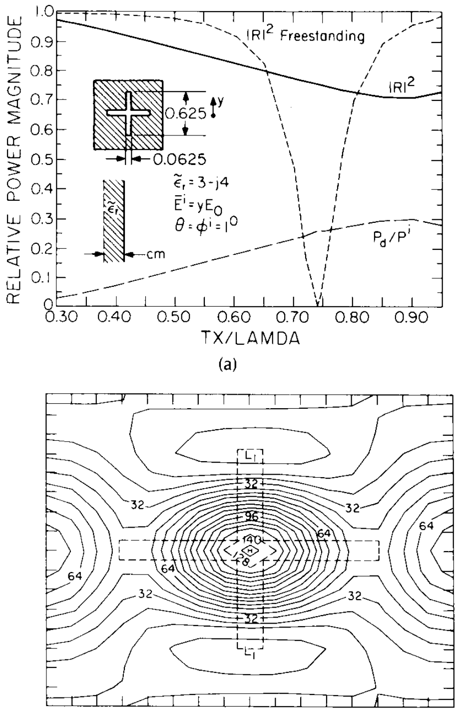

(a)

(b)

Fig. 22. Periodic surface backed by lossy dielectric layer. (a) Spectral response. (b) Contour plot of dissipated power.

slot is sketched on the plot. (The plot was elongated for reproduction.) The incident electric field is $\hat{y}$-directed—bottom to top on the page—producing a maximum electric field in the horizontal slot, peaking at the center. Hence, the dissipated power is maximum at the center with greater values along the horizontal slot as compared to that for the vertical slot.

G. Discussion of Results Derived by Using Cascade Approach

The cascade formulation has been presented as a means of cascading arbitrary elements to form a composite FSS. The scattering parameters of periodic surfaces and dielectric layers may be cascaded thus reducing the formulation from one that treats the entire structure to one that treats each element separately. This allows a simplification in the analysis as long as the number of harmonics calculated and included in the cascade connection was large enough to give an accurate solution. The cascade connection also allows a formal structuring of the fields which is used to calculate the spatial distribution of dissipated power within a lossy dielectric layer. In addition, more than one screen and dielectric layer can be cascaded.

The use of the Floquet harmonics to form the scattering parameters used in the cascade connection requires the calculation of the fields scattered from the periodic surface for multiple incident harmonics. The scattering parameters of the surface are then stored to be used with any combination of dielectric layers or other periodic surfaces. Hence, the calculation of the periodic surface scattering parameters must be easily performed for the cascade formulation to be efficient. This is in contrast to the formulations that analyze the screen in its entirety, where it is necessary to consider only a single incident harmonic. Therefore, where the cascade formulation gives the flexibility of treating a general screen, it does so at the expense of calculating the full set of surface scattering parameters.

VIII. FINITE AND CURVED FREQUENCY SELECTIVE SURFACES

In many practical applications of the FSS, it is sufficiently accurate to model it as a doubly-infinite, doubly-periodic, planar structure, that allows one to reduce the problem to one of finding the current (or aperture) distribution in just one cell rather than over the entire surface. However, there exist many other situations where it becomes necessary to account for the finite size of the FSS and to assess the effect of truncation in an accurate manner. Additionally, for many radome applications the FSS is curved, and except for some special geometry, e.g., a cylindrical surface, the FSS is no longer doubly-periodic. As a consequence of the truncation, or the presence of a finite curvature, the current distribution on each patch becomes an independent quantity. Thus one is forced to consider the problem in its entirety, and to simultaneously solve for the currents on the individual patches. Since the total number of patches is usually very large, the number of unknowns needed to generate the solution to the scattering problem of a finite or curved FSS with good accuracy can easily be on the order of several thousands, particularly if the subdomain basis functions are employed. Even with the entire domain basis functions, that are almost always used for such problems because of a significant reduction in the matrix size afforded by their choice, the size of the FSS that can be comfortably handled is relatively small. Consequently, it becomes necessary to employ certain approximations in order to render the truncated FSS problem a manageable one. This point is further elaborated on in the following.

Consider a finite, square FSS structure shown in Fig. 23. Let the number of patches in the x and y directions be N, where N may be large. As a first step, one breaks the finite FSS up into central, edge, and corner regions as shown in the figure. Next, one assumes that the currents in the central region of the finite FSS are essentially the same as they would be in a doubly-periodic, doubly-infinite FSS. As for an edge region, one assumes that the behavior of the currents near the edge is similar to the one that exists on the edge patches of a singly-truncated FSS (i.e., truncated in one direction and infinitely periodic in the other), one of whose edges coincides with the edge of the finite FSS under consideration. Obviously, a singly-truncated FSS is considerably more tractable in a numerically rigorous manner than is its doubly-truncated counterpart. Experience has shown that the edge effects become insignificant when one penetrates about seven or eight patches into the central region away from the edge. This may be seen by examining the results, given in Fig. 24, for the current distributions J_x's for a singly-truncated FSS with 31 cross-shaped patches in the x direction (see Fig. 23).

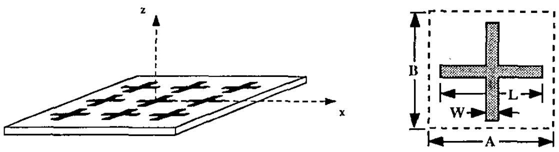

Fig. 23. A finite frequence selective surface. Currents are sampled along the $y = 0$, $z = 0$.

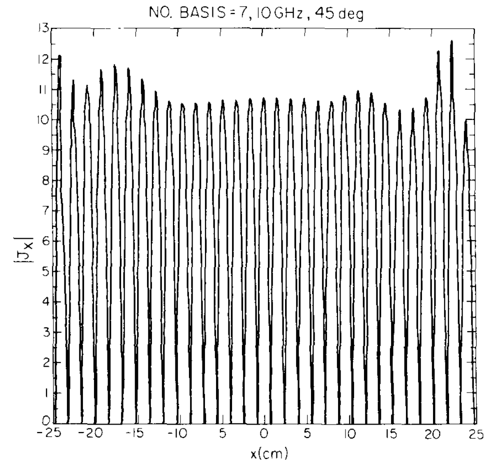

Fig. 24. Induced surface current on a finite-width frequency selective surface of 31 cross dipoles: TM polarization, $\theta = 45°$, frequency = 10 GHz.

Returning to the edge patches of the doubly-truncated FSS, one expresses the currents on these patches as superpositions of periodic and fringe solutions, the latter extracted from the solution of the singly-truncated geometry. Finally, the currents in the corner region can be approximated by a superposition of the three componenents, viz., the periodic, fringe, and corner currents. The last one must be extracted from the solution of a doubly-truncated FSS of manageable-size with, say, eight or so patches on the side.

Let us now identify a crucial difference between the way a doubly-periodic and singly- or doubly-truncated FSS are numerically analyzed [69]. Recall that for the doubly-periodic case the appropriate equation is (4), which, in turn, was derived from (3) after discretizing the transform variables α and β to α_{mn} and β_{mn}. When the FSS is truncated, the periodicity in the direction of the truncation is lost, and the summation must now be replaced by an integral over the continuous transform variable. (For the doubly-truncated case, both the transform variables become continuous.) The evaluation of the matrix elements containing integrals instead of summations becomes a considerably time-consuming process. Unfortunately, however, there is no short-cut approach that would circumvent this problem.

As for the arbitrary, curved-surface FSS problem, the situation can be even more complicated because, except for the special case of circularly cylindrical geometry, all periodicity is typically lost when the surface is no longer planar. Once again, to avoid having to deal with a very large number of unknowns, it becomes necessary to make suitable approximations, e.g., assuming that the surface is locally planar [69]. Under this approximation, one replaces the curved surface locally by a tangential planar surface. Next, one solves the doubly-infinite planar FSS problem for the above tangential surface, and uses this solution to approximate the current on the tangential patch on the curved surface. One then repeats the above procedure N times for each of the N patches to obtain the approximate current distribution on the entire curved FSS. One can also refine this approximate current by adding the fringe currents for the patches close to the edges, in the same manner as was done for the finite, planar FSS.

The techniques described above for the approximate analysis of doubly-truncated planar and curved FSS have been utilized recently by Merewether and Mittra [70] and Ko and Mittra [71], [72]. For further details the reader is referred to the above publications.

APPENDIX
OUTLINE OF ITERATIVE ALGORITHMS

The linear equation to be solved using the conjugate gradient (CG) technique is

$$\boldsymbol{L}\bar{J} = \bar{E}^i \tag{A1}$$

where $\bar{J}$ is the unknown current on the patch and $\bar{E}^i$ is the excitation field. The operator $\boldsymbol{L}$ though symmetric is not a positive/negative definite, self-adjoint operator. Without these properties, convergence cannot be guaranteed when applying the C-G technique. A positive definite, self-adjoint equivalent system may be formed by preoperating equation (A1) by the complex conjugate of the operator $\boldsymbol{L}^*$

$$\boldsymbol{L}^*\boldsymbol{L}\bar{J} = \boldsymbol{L}^*\bar{E}^i. \tag{A2}$$

A solution to (A2) is generated by using a given set of direction functions $\{\bar{d}_i\}_{i=1}^n$ which satisfy the following property

$$\langle \bar{d}_i, \boldsymbol{L}^*\boldsymbol{L}\bar{d}_j \rangle = 0, \qquad i \neq j \tag{A3}$$

where the inner product is defined as

$$\langle \bar{\phi}, \bar{\psi} \rangle = \int_{\partial s} \bar{\phi} \cdot \bar{\psi} \, ds,$$

and the norm is

$$\|\bar{\phi}\|^2 = \langle \bar{\phi}, \bar{\phi} \rangle.$$

Equation (A3) expresses the property that the set of direction functions is mutually conjugate, or simply orthogonal with respect to the operator $\boldsymbol{L}^*\boldsymbol{L}$. Expanding $\bar{J}$ in the basis $\{\bar{d}_i\}_{i=1}^n$ gives

$$\bar{J} = \alpha_1\bar{d}_1 + \alpha_2\bar{d}_2 + \alpha_3\bar{d}_3 + \cdots + \alpha_n\bar{d}_n \tag{A4}$$

where the scalars $\{\alpha_i\}_{i=1}^n$ are the unknown weighting coefficients. Substituting (A4) into (A2), premultiplying by $\bar{d}_i$, and applying the mutual conjugate property result in

$$\alpha_i \langle \bar{d}_i, \boldsymbol{L}^*\boldsymbol{L}\bar{d}_i \rangle = \langle \bar{d}_i, \boldsymbol{L}^*\bar{E}^i \rangle,$$

or

$$\alpha_i = \frac{\langle \bar{d}_i, \boldsymbol{L}^*\bar{E}^i \rangle}{\langle \bar{d}_i, \boldsymbol{L}^*\boldsymbol{L}\bar{d}_i \rangle}. \tag{A5}$$

The weighting coefficients have been found in terms of the unknown set of direction functions. This set is recursively generated using the C-G method.

Being an iterative process, the C-G technique successively generates the direction functions to minimize a prescribed error functional. In minimization of the integrated square error after application of the boundary conditions on the patch, the resultant error functional is

$$ERF^r(\bar{J}) = \|\bar{r}\|^2 \tag{A6}$$

which is minimization in the range of $\boldsymbol{L}$.

Minimizing the integrated square error in the difference between the exact current and an approximation for the current results in the error functional

$$ERF^d(\bar{J}) = \|\bar{J} - \bar{J}_e\|^2 \tag{A7}$$

where $\bar{J}_e$ is the exact current. This is minimization in the domain of $\boldsymbol{L}$. The algorithms that generate the direction functions and a solution for $\bar{J}$ are

RANGE	DOMAIN
$\bar{r}_0 = \boldsymbol{L}\bar{J}_0 - \bar{E}^i$	$\bar{r}_0 = \boldsymbol{L}\bar{J}_0 - \bar{E}^i$
$\bar{d}_0 = \boldsymbol{L}^*\bar{r}_0$	$\bar{d}_0 = \boldsymbol{L}^*\bar{r}_0$
$ERF_0^r = \|\bar{r}_0\|^2$	$ERF_0^d = \|\bar{r}_0\|^2$
$\alpha_n = \dfrac{\|\boldsymbol{L}^*\bar{r}_n\|^2}{\|\boldsymbol{L}\bar{d}_n\|^2}$ <<<<<<<	>>>> $\alpha_n = \dfrac{\|\bar{r}_n\|^2}{\|\bar{d}_n\|^2}$
$\bar{J}_{n+1} = \bar{J}_n + \alpha_n \bar{d}_n$	$\bar{J}_{n+1} = \bar{J}_n + \alpha_n \bar{d}_n$
$ERF_{n+1}^r = ERF_n^r = \dfrac{\|\boldsymbol{L}^*\bar{r}_n\|^4}{\|\boldsymbol{L}\bar{d}_n\|^2}$	$\bar{r}_{n+1} = \bar{r}_n - \alpha_n\boldsymbol{L}\bar{d}_n$
$\bar{r}_{n+1} = \bar{r}_n - \alpha_n\boldsymbol{L}\bar{d}_n$	$ERF_{n+1}^d = \|\bar{r}_{n+1}\|^2$

RANGE	DOMAIN
$\beta_n = \dfrac{\Vert \boldsymbol{L}^* \bar{r}_{r+1} \Vert^2}{\Vert \boldsymbol{L}^* \bar{r}_n \Vert^2}$	$\beta_n = \dfrac{\Vert \bar{r}_{n+1} \Vert^2}{\Vert \bar{r}_n \Vert^2}$
$\bar{d}_{n+1} = \boldsymbol{L}^* \bar{r}_{n+1} + \beta_n \bar{d}_n$	$\bar{d}_{n+1} = \boldsymbol{L}^* \bar{r}_{n+1} + \beta_n \bar{d}_n$
$n = n + 1$ loop >>>>>>>>>>	<<< loop $n = n + 1$.

ACKNOWLEDGMENT

The authors would like to take this opportunity to acknowledge helpful discussions and collaborative interactions over the past ten years with their colleagues at the University of Illinois and at a number of industrial organizations, including LTV Aerospace and Hughes Aircraft Company. Special thanks are due to K. Merewether of the University of Illinois and Dr. W. L. Ko of the University of South Florida for their contributions on finite and curved FSSs.

REFERENCES

[1] D. Rittenhouse, "An optical problem, proposed by Mr. Hopkinson, and solved by Mr. Rittenhouse," *Trans. Amer. Phil. Soc.*, vol. 2, pp. 201–206, 1786.

[2] F. O'Nians and J. Matson, "Antenna feed system utilizing polarization independent frequency selective intermediate reflector," U.S. Patent 3-231-892, Jan. 1966.

[3] C. H. Tsao and R. Mittra, "Spectral-domain analysis of frequency selective surfaces comprised of periodic arrays of cross dipoles and Jerusalem crosses," *IEEE Trans. Antennas Propagat.*, vol. AP-32, no. 5, pp. 478–486, May 1984.

[4] S. W. Lee, "Scattering by dielectric-loaded screen," *IEEE Trans. Antennas Propagat.*, vol. AP-19, no. 5, pp. 656–665, Sept. 1971.

[5] R. Ulrich, "Far-infrared properties of metallic mesh and its complementary structure," *Infrared Phys.*, vol. 7, pp. 37–55, 1967.

[6] M. S. Durschlag and T. A. DeTemple, "Far-IR optical properties of freestanding and dielectrically backed metal meshes," *Appl. Opt.*, vol. 20, no. 7, pp. 1245–1253, Apr. 1981.

[7] C. M. Horwitz, "A new solar selective surface," *Opt. Commun.*, vol. 11, no. 2, pp. 210–212, June 1974.

[8] W. H. Miller, G. D. Bernard, and J. L. Allen, "The optics of insect compound eyes," *Science*, vol. 162, pp. 760–767, 1968.

[9] G. H. Schennum, "Frequency-selective surfaces for multiple-frequency antennas," *Microwave J.*, pp. 55–57, May 1973.

[10] L. Young, L. A. Robinson, and C. A. Hacking, "Meander-line polarizer," *IEEE Trans. Antennas Propagat.*, vol. AP-21, pp. 376–378, 1973.

[11] J. A. Arnaud and F. A. Pelow, "Resonant-grid quasi-optical diplexers," *Bell Syst. Tech. J.*, vol. 54, no. 2, pp. 263–283, Feb. 1975.

[12] V. D. Agrawal and W. A. Imbriale, "Design of a dichroic Casegrain subreflector," *IEEE Trans. Antennas Propagat.*, vol. AP-27, no. 4, pp. 466–473, July 1979.

[13] R. H. Ott, R. G. Kouyoumjian, and L. Peters, Jr., "Scattering by a two-dimensional periodic array of narrow plates," *Radio Sci.*, vol. 2, no. 11, pp. 1327–1359, Nov. 1967.

[14] C. C. Chen, "Scattering by a two-dimensional periodic array of conducting plates," *IEEE Trans. Antennas Propagat.*, vol. AP-18, no. 5, pp. 660–665, Sept. 1970.

[15] ——, "Transmission of microwave through perforated flat plates," *IEEE Trans. Microwave Theory Tech.*, vol. MTT-21, no. 1, pp. 1–6, Jan. 1973.

[16] E. L. Pelton and B. A. Munk, "Scattering from periodic arrays of crossed dipoles," *IEEE Trans. Antennas Propagat.*, vol. AP-27, pp. 323–330, May 1979.

[17] C. H. Tsao, "Spectral-domain approach for analyzing scattering from frequency selective surface," Ph.D. Dissertation, University of Illinois, Urbana, IL, 1981.

[18] R. B. Kieburtz and A. Ishimaru, "Scattering by a periodically apertured conducting screen," *IRE Trans. Antennas Propagat.*, vol. AP-9, no. 6, pp. 506–514, Nov. 1961.

[19] C. C. Chen, "Transmission through a conducting screen perforated periodically with apertures," *IEEE Trans. Microwave Theory Tech.*, vol. MTT-18, no. 9, pp. 627–632, Sept. 1970.

[20] ——, "Diffraction of electromagnetic waves by a conducting screen perforated periodically with circular holes," *IEEE Trans. Microwave Theory Tech.*, vol. MTT-19, no. 5, pp. 475–481, May 1971.

[21] B. A. Munk, R. G. Kouyoumjian, and L. Peters, Jr., "Reflection properties of periodic surfaces of loaded dipoles," *IEEE Trans. Antennas Propagat.*, vol. AP-19, pp. 612–617, Sept. 1971.

[22] J. P. Montgomery, "Scattering by an infinite periodic array of thin conductors on a dielectric sheet," *IEEE Trans. Antennas Propagat.*, vol. AP-23, no. 1, pp. 70–75, Jan. 1975.

[23] R. J. Luebbers and B. A. Munk, "Some effects of dielectric loading on periodic slot arrays," *IEEE Trans. Antennas Propagat.*, vol. AP-26, no. 4, pp. 536–542, July 1978.

[24] ——, "Cross polarization losses in periodic arrays of loaded slots," *IEEE Trans. Antennas Propagat.*, vol. AP-23, pp. 159–164, Mar. 1975.

[25] T. Itoh, "Spectral domain immitance approach for dispersion characteristics of generalized printed transmission lines," *IEEE Trans. Microwave Theory Tech.*, vol. MTT-28, pp. 733–736, July 1980.

[26] K. M. Mitzner, "Effective boundary conditions for reflection and transmission by an absorbing shell of arbitrary shape," *IEEE Trans. Antennas Propagat.*, vol. AP-16, no. 8, pp. 706–712, Nov. 1968.

[27] R. C. Hall and R. Mittra, "Scattering from a periodic array of resistive strips," *IEEE Trans. Antennas Propagat.*, vol. AP-33, no. 9, pp. 1009–1011, Sept. 1985.

[28] R. Hall, "Electromagnetic scattering from periodic structures comprised of resistive sheet material," Ph.D. Dissertation, University of Illinois, Urbana, IL, 1986.

[29] T. A. Cwik and R. Mittra, "Scattering from a periodic array of free-standing arbitrarily shaped perfectly conducting or resistive patches," *IEEE Trans. Antennas Propagat.*, vol. AP-35, no. 11, pp. 1226–1234, Nov. 1987.

[30] R. F. Harrington, *Field Computation by Moment Methods.* New York, NY: Macmillan, 1968.

[31] R. Mittra and S. W. Lee, *Analytical Techniques in the Theory of Guided Waves.* New York, NY: MacMillan, 1971.

[32] R. Mittra, R. C. Hall, and C. H. Tsao, "Spectral-domain analysis of circular patch frequency selective surfaces," *IEEE Trans. Antennas Propagat.*, vol. AP-32, no. 5, pp. 533–536, May 1984.

[33] E. A. Parker and S. M. A. Hamdy, "Rings as elements for frequency selective surfaces," *Electron. Lett.*, vol. 17, no. 17, pp. 612–614, Aug. 1981.

[34] R. Cahill and E. A. Parker, "Concentric ring and Jerusalem cross arrays as frequency selective surfaces for a 45° incidence diplexer," *Electron Lett.*, vol. 18, no. 8, pp. 313–314, Apr. 1982.

[35] S. M. A. Hamdy and E. A. Parker, "Current distribution on the elements of a square loop frequency selective surface," *Electron. Lett.*, vol. 18, no. 14, pp. 624–626, 1982.

[36] R. Cahill and E. A. Parker, "Crosspolar levels of ring arrays in reflection at 45° incidence: influence of lattice spacing," *Electron. Lett.*, vol. 18, no. 24, pp. 1060–1061, 1982.

[37] R. J. Langley and E. A. Parker, "Double-square frequency-selective surfaces and their equivalent circuit," *Electron. Lett.*, vol. 19, no. 17, pp. 675–677, Aug. 1983.

[38] A. W. Glisson and D. R. Wilton, "Simple and efficient numerical methods for problems of electromagnetic radiation and scattering from surfaces," *IEEE Trans. Antennas Propagat.*, vol. AP-28, no. 5, pp. 593–603, Sept. 1980.

[39] B. J. Rubin and H. L. Bertoni, "Reflection from a periodically perforated plane using a subsectional current approximation," *IEEE Trans. Antennas Propagat.*, vol. AP-31, no. 6, pp. 829–836, Nov. 1983.

[40] T. Cwik, "Scattering from general periodic screens," Ph.D. Dissertation, University of Illinois, Urbana, IL, 1986.

[41] C. H. Chan, "Investigation of iterative and spectral Galerkin techniques for solving electromagnetic boundary value problems," Ph.D. Dissertation, University of Illinois, Urbana, IL, 1987.

[42] R. Mittra, "Relative convergence of the solution of a doubly infinite set of equations," *J. Res. Nat. Bur. Stand.*, vol. 67D, no. 2, pp. 245–253, Mar.-Apr. 1963.

[43] S. W. Lee, W. R. Jones, and J. J. Campbell, "Convergence of numerical solutions of iris-type discontinuity problems," *IEEE Trans. Microwave Theory Tech.*, vol. MTT-19, no. 6, pp. 528–536, June 1971.

[44] R. Mittra, T. Itoh, and T. S. Li, "Analytical and numerical studies of the relative convergence phenomenon arising in the solution of an integral equation by moment method," *IEEE Trans. Microwave Theory Tech.*, vol. MTT-20, no. 2, pp. 96–104, Feb. 1972.

[45] N. Shuley, "A note on relative convergence for moment-method solutions of integral equations of the first kind as applied to dichroic problems," *Electron Lett.*, vol. 21, no. 3, pp. 95–97, 1985.

[46] L. W. Pearson, "A technique for organizing large moment calculations for use with iterative solution methods," *IEEE Trans. Antennas Propagat.*, vol. AP-33, pp. 1031–1033, Sept. 1985.

[47] M. R. Hestenes and E. Stiefel, "Methods of conjugate gradient for solving linear systems," *J. Res. Nat. Bur. Stand.*, vol. 49, no. 6, pp. 409–436, Dec. 1952.

[48] P. M. van den Berg, "Iterative computational techniques in scattering based upon the integrated square error criterion," *IEEE Trans. Antennas Propagat.*, vol. AP-32, no. 10, pp. 1063–1070, Oct. 1984.

[49] A. Kas and E. L. Yip, "Preconditioned conjugate gradient methods for solving electromagnetic problems," *IEEE Trans. Antennas Propagat.*, vol. AP-35, pp. 147–152, Feb. 1987.

[50] J. P. Montgomery and K. R. Davey, "The solution of planar periodic structures using iterative methods," *Electromagnetics*, vol. 5, nos. 2–3, pp. 209–235, 1985.

[51] C. G. Christodoulou and J. F. Kauffman, "On the electromagnetic scattering from infinite rectangular grids with finite conductivity," *IEEE Trans. Antennas Propagat.*, vol. AP-34, pp. 144–154, Feb. 1986.

[52] J. P. Montgomery, "Scattering by an infinite periodic array of thin conductors on a dielectric sheet," *IEEE Trans. Antennas Propagat.*, vol. AP-23, no. 1, pp. 70–75, Jan. 1975.

[53] L. L. Tasi, T. K. Wu, and J. T. Mayhan, "Scattering by multilayered lossy periodic strips with application to artificial dielectrics," *IEEE Trans. Antennas Propagat.*, vol. AP-26, no. 2, pp. 257–260, Mar. 1978.

[54] T. K. Wu, "Analysis and application of multilayered periodic strips," *AEU*, vol. 33, no, 4, pp. 144–148, 1979.

[55] R. J. Luebbers and B. A. Munk, "Mode matching analysis of biplanar slot arrays," *IEEE Trans. Antennas Propagat.*, vol. AP-27, no. 3, pp. 441–443, 1979.

[56] M. A. A. El-Morsy, E. A. Parker, and R. J. Langley, "4 layer inductive grid FSS at 45° incidence," *Electron Lett.*, vol. 19, no. 16, pp. 602–603, 1983.

[57] L. Henderson, "The scattering of planar arrays of arbitrarily shaped slot and/or wire elements in a stratified dielectric medium," Ph.D. Dissertation, The Ohio State University, Columbus, OH, 1983.

[58] E. C. DuFort, "Finite scattering matrix for an infinite antenna array," *Radio Sci.*, vol. 2, no. 1, pp. 19–27, Jan. 1967.

[59] S. Contu and R. Tascone, "Scattering matrix of passive arrays in a stratified dielectric," *CSELT Rapporti Tecnici*, vol. XI, no. 6, pp. 361–364, Dec. 1983.

[60] N. V. Shuley, "Higher-order mode interaction in planar periodic structures," *Proc. IEE-H*, vol. 131, no. 3, pp. 129–132, June 1984.

[61] C. C. Chen, "Transmission of microwave through perforated flat plates of finite thickness," *IEEE Trans. Microwave Theory Tech.*, vol. MTT-21, pp. 1–6, Jan. 1973.

[62] B. A. Munk, R. J. Luebbers, and R. D. Fulton, "Transmission through a two-layer array of loaded slots," *IEEE Trans. Antennas Propagat.*, vol. AP-22, pp. 804–809, Nov. 1974.

[63] B. A. Munk and R. J. Luebbers, "Reflection properties of two-layer dipole arrays," *IEEE Trans. Antennas Propagat.*, vol. AP-22, pp. 766–773, Nov. 1974.

[64] N. Shuley, "Analysis of dichroic surfaces," Ph.D. Dissertation, Chalmers University of Technology, Gothenburg, Sweden, Jan. 1985.

[65] S. W. Lee, "Scattering by dielectric-loaded screen," *IEEE Trans. Antennas Propagat.*, vol. AP-19, no. 5, pp. 656–665, Sept. 1971.

[66] T. Cwik and R. Mittra, "The cascade connection of planar periodic surfaces and lossy dielectric layers to form an arbitrary periodic screen," *IEEE Trans. Antennas Propagat.*, vol. AP-35, pp. 1397–1405, Dec. 1987.

[67] N. Amitay, V. Galindo, and C. P. Wu, *Theory and Analysis of Phased Array Antennas*. New York, NY: Wiley, 1972, pp. 310–313.

[68] D. M. Sazanov, A. N. Gridin, and B. A. Michustin, *Microwave Circuits*. Moscow: Mir, 1982, pp. 154–178.

[69] T. Cwik and R. Mittra, "The effects of the truncation and curvature of periodic surfaces: A strip grating," *IEEE Trans. Antennas Propagat.*, vol. AP-36, pp. 612–622, May 1988.

[70] K. Merewether and R. Mittra, "Spectral domain analysis of a finite frequency-selective surface with cross-shaped conducting patches," presented at IEEE-AP-S Int'l Symposium, June 1988.

[71] W. L. Ko and R. Mittra, "Scattering by a truncated periodic array," *IEEE Trans. Antennas Propagat.*, vol. AP-36, pp. 496–503, Apr. 1988.

[72] ——, "Scattering by a conformal array of metallic patches," to be published.

Raj Mittra (Fellow, IEEE) received the M.S. degree in radiophysics from the University of Calcutta, India, and the Ph.D. degree in electrical engineering from the University of Toronto, Ontario, Canada.

He is the Director of the Electromagnetic Communication Laboratory of the Electrical and Computer Engineering Department and Research Professor of the Coordinated Science Laboratory at the University of Illinois, Urbana. He is President of RM Associates, which is a consulting organization providing services to several industrial and governmental organizations. His professional interests include the areas of analytical and computerated electromagnetics, high speed digital circuits, radar scattering, satellite antennas, microwave and millimeter wave integrated circuits, frequency selective surfaces, EMP and EMC analysis, and remote sensing.

Dr. Mittra is a past President of the IEEE Antennas and Propagation Society, and has served as Editor of the IEEE TRANSACTIONS ON ANTENNAS AND PROPAGATION.

Chi H. Chan (Member, IEEE) was born in Macao on April 16, 1959. He attended Hong Kong Polytechnic and the City College of New York. He received the B.S. and M.S. degrees in electrical engineering from the Ohio State University, Columbus, in 1981 and 1982, respectively, and the Ph.D. degree in electrical engineering from the University of Illinois, in 1987.

From 1981 to 1982, he was a Graduate Research Associate at the ElectroScience Laboratory, Ohio State University. Since August 1982, he has been with the Electromagnetic Communication Laboratory in the Department of Electrical and Computer Engineering at the University of Illinois, Urbana, where he is presently a Visiting Assistant Professor. His research interests include numerical techniques in electromagnetics, scattering from electrically large bodies, frequency-selective surfaces, microwave integrated circuits, high-speed digital circuits, and integrated optics.

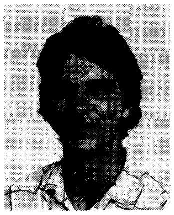

Tom Cwik was born in Chicago, IL, on July 4, 1957. He received the B.S., M.S., and Ph.D. degrees in electrical engineering from the University of Illinois, Urbana-Champaign, in 1979, 1981, and 1986, respectively.

After receiving the M.S. degree, he spent a summer as an assistant at the Very Large Array, National Radio Astronomy Laboratory in Socorro, NM. Following this he spent a year with the National Bureau of Standards in Boulder, CO. Upon completion of the Ph.D. degree he was a postdoctoral fellow at ELAB, The Norwegian Institute of Technology in Trondheim, Norway. Currently he is a member of the technical staff at the Jet Propulsion Laboratory, California Institute of Technology, Pasadena. His interests include wave scattering, frequency selective surfaces, the application of parallel processing to electromagnetic problems, and asymptotic analysis in reflector systems.